



## **D6.10 Release of the general Italian NBS database and related services, including results of the UAV fleet used for selected NBS**

### **MAIN AUTHORS**

**Alice Baronetti, Andrea Berton, Letizia Costanza,  
Davide Cini, Antonello Provenzale**



<b>Deliverable number:</b>	D6.10
<b>Work package:</b>	WP6 – Terrestrial Biosphere
<b>Intermediate Objective:</b>	*****
<b>Deliverable type:</b>	X Document, report
	<input type="checkbox"/> Websites, patent filings, videos, etc.
	<input type="checkbox"/> Other: please specify .....
<b>Dissemination level:</b>	X Public
	<input type="checkbox"/> Restricted
<b>Estimated delivery (bimester):</b>	B13
<b>Actual delivery date:</b>	30/12/2024
<b>Author(s) (Partner-OU):</b>	Antonello Provenzale (CNR IGG), Andrea Berton (CNR IGG), Letizia Costanza (CNR IGG), Davide Cini (CNR IGG), Alice Baronetti (CNR IGG)
<b>Reviewed by:</b>	ITINERIS Executive Board
<b>Note:</b>	

*IR0000032 – ITINERIS, Italian Integrated Environmental Research Infrastructures System - CUP B53C22002150006 (D.D. n. 130/2022)  
Funded by EU - Next Generation EU  
Mission 4 “Education and Research” - Component 2: “From research to business” -  
Investment 3.1: “Fund for the realisation of an integrated system of research and innovation infrastructures”*

## Summary

<b>1</b>	<b>STATE OF ART AND RESEARCH QUESTIONS</b>	<b>4</b>
<b>1.1</b>	<b>Drought and Vegetation</b>	<b>4</b>
<b>1.2</b>	<b>Remote sensing</b>	<b>5</b>
<b>2</b>	<b>ACTIVITIES AND RESULTS</b>	<b>7</b>
<b>2.1</b>	<b>Drought and vegetation</b>	<b>7</b>
2.1.1	Study area: northern Italy	7
2.1.2	Data and Method	9
2.1.3	Result and discussion	12
<b>2.2</b>	<b>Unmanned Aerial Vehicle (UAV) for remote sensing</b>	<b>21</b>
2.2.1	Songbird 150 Specifications and flight performance:	21
2.2.2	Songbird 150 Sensor	31
2.2.3	Songbird 150 Ground Control Station and Mission Planning	33
2.2.4	Songbird 150 Functions	36
2.2.5	Songbird 150 Head-up Display and Telemetry	39
2.2.6	Songbird 150 Assembly:	41
2.2.7	Songbird 150 ADS-B System	43
2.2.8	Mobile Research Unit	44
2.2.9	Data and Method	47
<b>3</b>	<b>CONCLUSION</b>	<b>56</b>
<b>4</b>	<b>BIBLIOGRAPHY</b>	<b>57</b>

## 1 STATE OF ART AND RESEARCH QUESTIONS

The ITINERIS project provides an opportunity to develop a service that promotes Nature-Based Solutions (NBS) to mitigate environmental pressures from climate change. In fact, the impact of human activities has reached a level that could lead to abrupt and, possibly, irreversible environmental changes that would significantly affect human well-being. This requires a change in the technologies that should support nature instead of damage it. In this framework, the project is focused on a specific aspect of NBS, based on the investigation of the effects of drought severe events devoted to limitate biodiversity and vegetation losses.

The effectiveness of such solutions is then implemented by means of high resolution remote sensing images of the environmental conditions using drone measurements of the landscape and vegetation conditions. In fact, non-disruptive digital technologies are useful to investigate the adaptation and resilience of ecological systems to climate change and extreme weather events. To achieve this, drone sensors that combine 3D vision with multispectral imaging were adopted to capture high-quality, precise digital parameters in real time.

This drone equipment is then complemented by the state-of-the-art user guide which illustrates the methodology to obtain several land products (as LST, Digital Elevation Model and Vegetation Indices). The use of drone technology significantly enhances the investigation of how specific ecosystems respond to climate change. Drone provides real-time, high-resolution images that surpass the lower-resolution data available from the actual satellites.

### 1.1 Drought and Vegetation

In the Mediterranean Basin, the large annual variability of rainfall is a primary factor contributing to the intensification of droughts (Lionello, 2012). These drought events has several negative impacts on human activities and ecosystems as: crop yield losses (Schillinger et al., 2008), forest fires (Turco et al., 2018), vegetation degradation (Rodrigo Comino et al., 2022), and desertification (Halbac-Cotoara-Zamfir et al., 2020). Assessing the impact of droughts on vegetation greenness is complicated by the complexity of the Mediterranean landscapes and also vegetation communities are adapted to frequent droughts with various morphological and phenological strategies (Fernández-Manjarrés et al., 2018). However, human activities have altered the Mediterranean ecosystem, affecting native vegetation communities and their resilience to drought events.

Northern Italy, entirely situated within the Mediterranean Basin, is predominantly characterised by a temperate climate, making it rich in water resources historically. However, in recent years, the frequency of drought events has increased, with a significant rise in the duration of the Po River's lean period since 2000. The dry and hot conditions experienced in 2003, 2010, 2017, 2019, and 2022 have significantly impacted both the lean period of the Po River and agricultural production. In particular, due to the complexity of this climatic condition, each drought event is characterised by specific climate conditions

and triggering factors. For instance, the intense heatwave of summer 2003 has generated a particularly severe drought event, where the main contributing factors were the rise in extreme high temperatures due to anticyclonic conditions, and a positive soil moisture anomaly in late spring.. The summer temperature anomaly for 2003 was +0.46 °C compared to the reference period of 1961-1990 (Luterbacher et al., 2004). More recently, northern Italy has faced severe and persistent drought conditions since early 2022, driven by extremely low precipitation levels and early heatwaves in May and June (European Drought Observatory, 2022).

In this context, it is essential to view droughts as the result of water stress, generated by low precipitation rates and high evaporative demand. Remote sensing data plays a crucial role in addressing this issue. Unlike meteorological stations, which offer localized measurements, remote sensing provides spatially continuous data even in complex regions like the Mediterranean basin and northern Italy (Astiasari et al., 2020). Numerous studies have utilised remote sensing data to analyse the impact of drought events on natural vegetation and crops in the Mediterranean basin. Notable examples include the research by Vicente-Serrano et al. (2019) in northeast Spain, Gouveia et al. (2012) in Portugal and Karnieli et al. (2019) across Europe.

On the other hand in literature there is a lack of studies based long-term remote sensing observations of vegetation response in northern Italy. To this end, according to the main goal to promote Nature-Based Solutions (NBS) to mitigate environmental pressures from climate change, the drought risk maps for northern Italy were produced and provided. These maps illustrate vegetation communities' response to medium- and long-term drought episodes.

## 1.2 Remote sensing

With the application of microelectronics to robotics, the first remote-controlled systems were divided into two types: fixed-wing and multicopter. In both cases, these aircraft are capable of flying close to the ground. In 2022, the EU drew up two regulations, 2019/947 and 2019/945, establishing a framework for the safe operation of civilian drones in European airspace. These regulations adopt a risk-based approach, taking into account the weight and the features of the civil drone and the operation it intends to carry out.

Regulation (EU) 2019/947 addresses most types of civil operations made by drones and their associated risk levels. It defines three categories of civil drone operations: "open," "specific," and "certified." The open category favors the use of small, lightweight drones, allowing the application of these instruments for scientific studies in remote environments, such as high mountains or the Arctic. However, these systems have operational limitations due to their low endurance and poor stability in adverse weather conditions. While, in the study of large-scale ecosystems, it is necessary to use larger drones with significant flight autonomy, such as fixed-wing models.

The use of modern drones enables an increase of the spatial resolution in remote sensing, starting from satellites, moving to aerial surveys, and finally reaching drone

capabilities. Drone technology significantly has improved the study of specific ecosystems in response to climate change. Drones provide real-time, high-resolution images that surpass the low-resolution data available from traditional satellites. In the study of complex ecosystems, using drones optimizes the timing of data acquisition for effective use of the onboard sensors.

## 2 ACTIVITIES AND RESULTS

In the following section the results on the study of the drought effects on the vegetation greenness in northern Italy and the application of an innovative drone instrumentation were described.

### 2.1 Drought and vegetation

The goal of the study is to produce high resolution risk maps of drought to illustrate spatial distribution of vegetation communities and their response to medium- and long-term drought episodes.

#### 2.1.1 Study area: northern Italy

According to the main goal of ITINERIS WP6 Task 6.15 northern Italy was chosen as our study case (Figure 1).

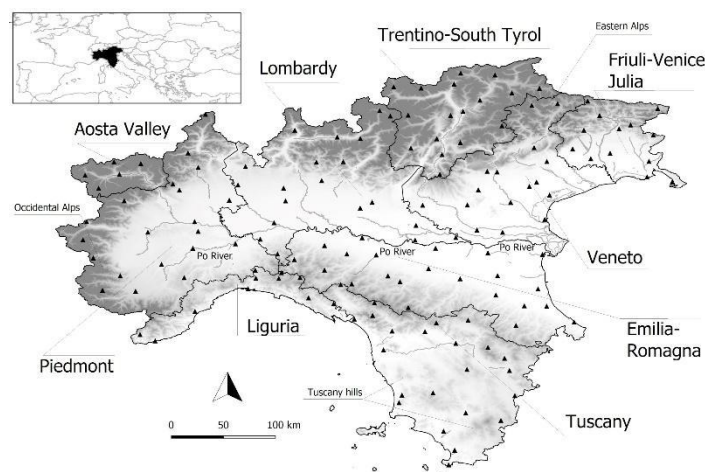


Figure 1: Study area and location of the 150 meteorological ground station

The region is made of nine administrative regions: Aosta Valley, Piedmont, Liguria, Lombardy, Emilia-Romagna, Veneto, Friuli-Venezia Giulia, Trentino-Alto Adige/Südtirol, and Tuscany. The area is made of the Po valley, surrounded by the Alps to the north and northwest, the Tuscan-Emilian Apennines to the south, and the Adriatic Sea to the east. The Valley represents 71% of all Italian plains, and it is crossed eastward by the Po river, which, with its 652 km, is the longest Italian river. The Po Basin, with its area of 1,327 km<sup>2</sup>, has numerous tributaries originating from the Alps and the Apennines. Po Valley is one of the most fertile areas in Italy and intensive agriculture dominates 41% of the Po Plain's land use. In fact counts 4,568,837 hectares of cultivated land, with 59% of it being irrigated (ISTAT, 2015). The main crops in irrigated areas include grain corn (32.5%), rice (14.5%), and vegetables (38.3%). In the northern part of the river basin, 85% of the area is dedicated to irrigated agriculture, with fruit trees (4.5%), industrial crops (4.2%), and open field vegetables (3.58%, Musolino et al., 2017). Natural vegetation in the lowlands is mainly made of mixed broadleaf forests, while in the Alps and Apennines the variability is highly

influenced by the altitude. It starts with deciduous trees, then above the forests lies a band of evergreen needleleaf trees, which are eventually replaced by shrubs at higher elevations. Beyond the shrubs, the typical biome consists of Alpine grasslands and tundra (Figure 2).

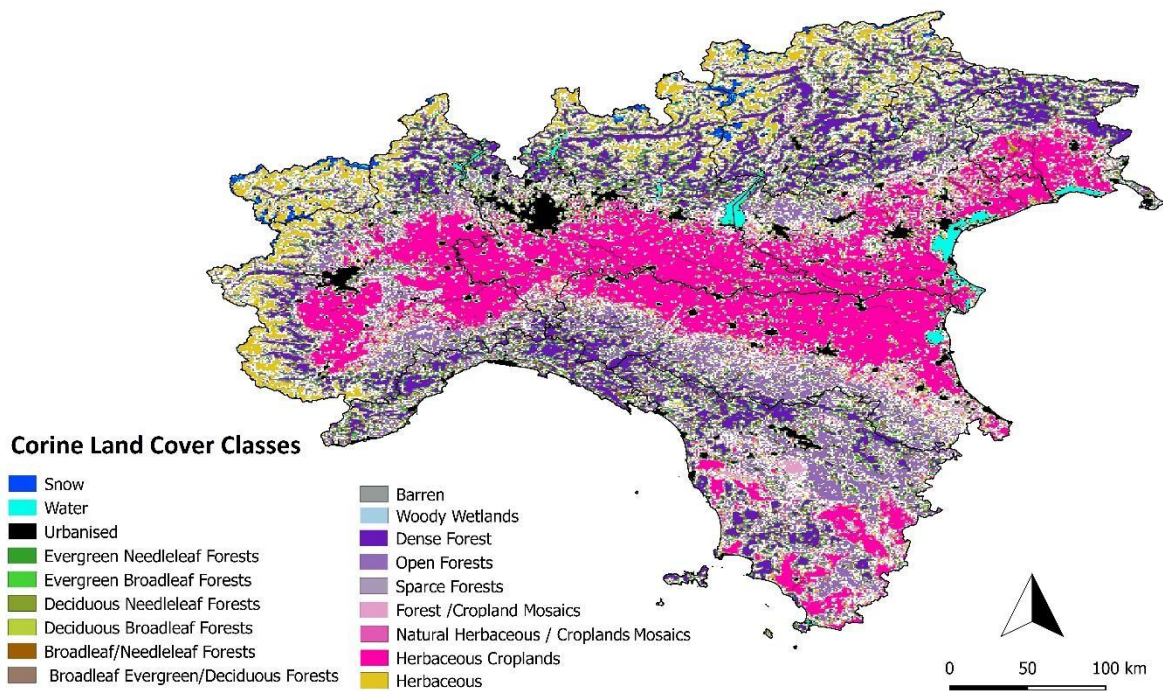


Figure 2: MODIS Corine Land Cover 2020 (MCD12Q1) for northern Italy

### Northern Italy climate

Northern Italy, even if it completely falls in the Mediterranean basin, is mainly characterised by a temperate climate. Alps and Apennines act as barriers to the main winds exposing the region to different circulation types. For instance the Alps protect the Po Valley from cold currents coming from the north. In fact, the orography promotes the formation of foehn winds, which are dry and warm katabatic winds caused by a pressure difference of 4 to 8 hPa between the upwind and downwind sides of the Alps (Fратиanni et al., 2009). Additionally, the Mediterranean Sea has a mitigating effect, promoting the formation of low pressure systems (cyclogenesis) near the Italian peninsula, leading to extreme precipitation events along the Ligurian coast. Three are the rainiest sectors (Figure 3): Easter Alps (Julian and Carnian Alps) with annual precipitation amount between 2500 and 3000 mm, the Tuscan-Emilian Apennines where are reached 2300 mm of precipitation per year and the Occidental Alps with an annual average of total precipitation between 1700 and 2000 mm (Fратиanni & Acquaotta, 2017).

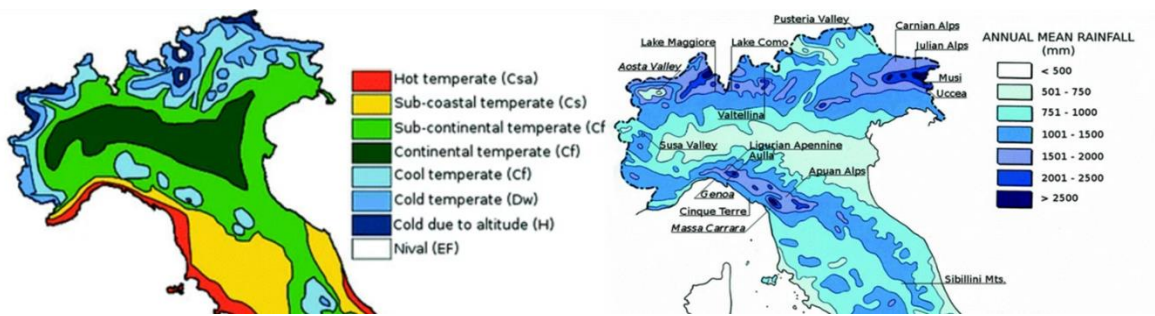


Figure 3: Climate of northern Italy: in the right part are displayed the main Köppen climate types, in the left the spatial distribution of the cumulate annual precipitation amount (Modified by Fratianni & Acquotta 2017).

According to the Köppen classification (Figure 3), the main climate observed in the Po Valley and at the foothills are hot summer temperate climate (Cfa) and lukewarm summer temperate climate (Cfb, Vallorani et al., 2018). Winters are cold and dry, with mean temperature in the colder month between  $-1^{\circ}\text{C}$  and  $4^{\circ}\text{C}$ , and temperature inversions are frequent. Summers are hot, with temperature recorded in July ranging from  $22^{\circ}\text{C}$  and  $24^{\circ}\text{C}$ . This is the driest sector with annual precipitation between 600 to 800 mm (Bigi et al., 2012).

Along the Ligurian coastal regions a hot temperate (Csa) is observed while a sub-coastal temperate (Cs) in the hilly zones of the Tuscany region (Figure 3). The Csa climate is characterised by summer droughts. During the coldest month temperature are ranging from 6 to  $9.9^{\circ}\text{C}$  and for four months temperature surpass the  $20^{\circ}\text{C}$ . For the internal sub-coastal region (Cs) climate the mean temperature recorded during the coldest month is between 4 and  $5.9^{\circ}\text{C}$ , and for three month temperature are greater than  $20^{\circ}\text{C}$ .

In the mountainous regions, a cold temperate climate (Dw, Figure 3) prevails, with mean annual temperatures between  $3^{\circ}\text{C}$  and  $5.9^{\circ}\text{C}$  (Nigrelli et al., 2018). Snowfall is common in winter and early spring, averaging 20–50 cm annually. However, some Alpine valleys, enclosed by high mountain peaks that influence local circulation, experience significantly lower precipitation, with monthly totals as low as 30–40 mm (Diodato et al., 2021).

## 2.1.2 Data and Method

### 2.1.2.1 Data

Remote sensing images: MODIS product

The remote sensing datasets utilised in this study belong to the MODIS Terra Collection 6. These data were sourced from the NASA/USGS Land Resources Distributed Active Archive Center (LP DAAC). In detail, 16-day vegetation indices (MOD13A2), representing the Normalized Difference Vegetation Index (NDVI) and Enhanced Vegetation Index (EVI) were downloaded at a spatial resolution of  $1 \times 1 \text{ km}^2$  for the period from March 1, 2000, to August 31, 2021.

Data were obtained for the months from March to August, in order to detect the vegetation growing season in northern Italy, avoiding interference from winter snow cover. The observed rise in temperatures over recent decades (Ceppi et al., 2012) has notably influenced the growing season's duration in Italy. The Joint Research Centre of the European Union reported an extension in the period between the last spring frost and the first autumn frost, ranging from 0.2 to 0.6 days per year (source: European Environment Agency).

Quality control was then applied, excluding all low-quality pixels, including those with no data or cloud coverage. Urban areas and waterbodies were identified and masked using land cover maps from the European Environmental Agency's CORINE program and the MODIS MCD12Q1 product.

#### Ground data

The National System for the Collection, Processing, and Dissemination of Climatic Data of Environmental Interest (SCIA) database is managed by the Italian Institute for Environmental Protection and Research (ISPRA) and, since the 2006, the database provides quality-controlled climatic data derived from national and regional meteorological networks spread on the National territory. In the following study 150 daily precipitation and 150 daily maximum and minimum dataset for the common period from March 1, 2000, to August 31, 2020 were downloaded from the SCIA database and quality controlled.

The first step of quality control consists in the check of the data series continuity and only daily precipitation and temperature series with less than 10% of gaps were retained. Then the detection of digitising errors in both temperature and precipitation series was performed. Were flagged as errors (and deleted) records as daily minimum temperature greater or equal to maximum temperature and daily negative precipitation values. Daily outliers were also flagged but not deleted. Were considered outliers, weekly precipitation accumulation amounts erroneously recorded as single-day values. While for temperature, values exceeding the  $\pm$  four standard deviations were flagged as suspicious. At the same time a visual quality check was performed, plotting daily precipitation and temperature data to identify outliers (Aguilar et al. 2005). The observed outliers were tested comparing the records of the surrounding meteorological stations and then flagged.

To align the dataset with remote sensing products, the quality controlled daily data were cumulated (for precipitation) or averaged (for temperature) into bi-weekly (16-day) series. Since the calculation of drought indices requires uniform time intervals, and to avoid the problem of leap years, each month was divided into two fixed periods: the 1st to the 16th and the 17th to the month's end.

Then the gap-filling approach to reconstruct the fragmented bi-weekly series (candidate) was adopted as the second step of quality control, and it was conducted using the average values from nearby stations (Reference, González-Hidalgo et al., 2018). Reference series were chosen following two conditions: elevation differences of less than 100 meters and distances within 20 kilometres between the candidate and reference stations (Baronetti et al., 2020). Correlation analysis between candidate and potential reference series was performed using the statistical methods described in the Co.Rain (for precipitation, Guenzi et al., 2017) and Co.Temp (for temperature) R packages, originally designed to identify discontinuities in precipitation (or temperature) series caused by changes in measurement instruments. It is adopted to compare measurements made with an old instrumentation (candidate) with those made with a new one (reference). This approach employs several statistical methods such as root mean square error (RMSE) to evaluate differences and similarities between series. All nearby stations meeting the criteria were considered as references for gap-filling.

The reconstructed bi-weekly series for precipitation and temperature were then interpolated using the geostatistical method of the Universal Kriging. A spatial resolution of  $1 \times 1 \text{ km}^2$  was adopted to match the MODIS imagery grid, with the area defined by WGS84 coordinates: North 47.20, South 42.29, West 6.56, and East 13.98. Considering the variability in station locations and elevations, auxiliary predictors, such as latitude, longitude, elevation, and distance to the shoreline, were incorporated to calculate kriging weights (Baronetti et al., 2020).

### 2.1.2.2 Method

According to the main goal to provide drought risk maps for northern Italy, main drought events and the simplified water balance, calculated as the difference between precipitation and potential evapotranspiration (PET), were investigated. Firstly the PET was estimated and, among the several techniques, the most recommended is the FAO–Penman–Monteith (FAO-PM) developed by the Food and Agriculture Organization (FAO) and the World Meteorological Organization. However, this method is based on numerous meteorological variables that are often unavailable in historical datasets (Shirmohammadi-Aliakbarkhani & Saberli, 2020).

The Hargreaves and Samani (HG) method (Hargreaves & Samani, 1985), is also adopted to estimate evapotranspiration and it is widely used in Mediterranean regions like Spain (García-Garizábal et al., 2014), Greece (Kitsara et al., 2013), and Italy (Pavanelli & Capra, 2014). This is the chosen method for our study and it is simpler than the FAO-PM. Vicente-Serrano et al. (2014) specifically recommended the HG for estimating potential evapotranspiration in the Mediterranean basin with a limited availability of meteorological data. The HG method uses mean temperature (T) and solar radiation (Rs) and is expressed as:

$$PET = R_e \times 0.0135 \times k_{RS} \times (T + 17.8) \times \Delta T^{0.5}$$

Here,  $R_e$  represents solar radiation (equivalent evaporation in mm/day),  $k_{RS}$  is the empirical radiation adjustment coefficient ( $^{\circ}\text{C}^{-0.5}$ ),  $\Delta T$  is the temperature difference ( $T_{\text{max}} - T_{\text{min}}$ ) and T is mean temperature ( $(T_{\text{max}} + T_{\text{min}})/2^{\circ}\text{C}$ ). For this study,  $k_{RS}$  was set to  $0.16 \text{ }^{\circ}\text{C}^{-0.5}$  as recommended for interior continental regions (Allen et al., 1998).

Once the PET was calculated on the defined cell grid, drought conditions were assessed using the Standardized Precipitation Index (SPI) and the Standardized Precipitation Evapotranspiration Index (SPEI). SPI evaluates droughts based on precipitation deficits only (McKee et al., 1993), while SPEI considers both precipitation and PET, providing a comprehensive information about the climate balance between water supply and water demand of a system rich in vegetation (Vicente-Serrano et al., 2010). Both indices detect drought period (negative values) and wet period (positive values) at several aggregation timescales (from 1 or 3 months for short episodes to 24 or 48 months for long events, Tirivarombo et al., 2018). In the following study the indices were calculated at medium (12 months) and long (24 and 36 months) aggregation timescales using the SPEI R package (Beguería et al., 2017). Drought episodes were then classified according to criteria adapted for the Mediterranean region by Baronetti et al. (2020) and González-Hidalgo et al. (2018):

a minimum length of four consecutive weeks, coverage of at least 25% of the study area, and severity thresholds, with severe droughts defined by index values between  $-1.65$  and  $-1.28$ , and extreme droughts by values  $<-1.65$ . The detected bi-weekly drought at medium and long time scales were then analysed to identify their starting and ending weeks, as well as their magnitude, duration, and percentage of area affected. To this end maps of the spatial distribution of the longest severe and extreme droughts were produced. Differences between SPI and SPEI results were quantified also as the difference between the percentage of area under drought detected by each index, with negative values indicating SPI drought events more spatially extended than SPEI and vice-versa.

Then to obtain maps that highlight areas mostly interest by droughts intensification and vegetation stress, trends of bi-weekly drought (using SPEI and SPI indices) and vegetation (NDVI and EVI) indices were evaluated using the Mann–Kendall test (Mann, 1945) at a pixel level. The statistical significance was set at 95%. Water balance maps for drought and non-drought conditions during spring, summer, and the growing season were generated to visualise differences through the time and the geographic areas.

To assess vegetation response to drought, correlation maps that figure out the impact of drought in vegetation greenness were generated, calculating the Pearson's correlation coefficient ( $r$ ) between bi-weekly vegetation indices (NDVI and EVI) and drought indices (SPEI and SPI), at medium (12 months) and long (24 and 36 months) aggregation timescales. Only the significant ( $p$  value  $<0.05$ ) and strongest ( $-0.6 < r > 0.6$ ) correlations were retained (Gouveia et al., 2017). Finally, the main vegetation types in northern Italy were identified using the CORINE Land Cover MODIS product. The drought impacts on vegetation were estimated for medium and long timescales. For each vegetation type, the Pearson's correlation coefficients between SPEI/SPI and NDVI/EVI were calculated. The percentage of vegetation affected by drought was then determined. This percentage was defined as the proportion of grid points occupied by a specific vegetation type with significant and strong correlations, relative to the total number of grid points for that vegetation type.

### *2.1.3 Result and discussion*

The Mediterranean basin is a climate change hotspot and a crucial region for studying droughts (Longobardi et al., 2016). In Italy, significant efforts have focused on investigating droughts in central and southern regions, driven by a significant decrease of annual precipitation since the mid-20th century (Sirangelo et al., 2017). While northern Italy is historically rich of water resources area, that in the last 20 years has experienced severe drought events. Despite this, few studies have addressed drought in this region (Baronetti et al., 2020; Marchina et al., 2017). Therefore, it is essential to improve the knowledge of droughts in northern Italy, with a particular focus on its severity and its impacts on ecosystems and vegetation communities. To this end the following study aims to provide drought risk maps for northern Italy, highlighting the spatial distribution of drought severity and the response of vegetation communities to medium- and long-term drought episodes.

#### *2.1.3.1 Drought events*

The investigation of summer and spring drought events for the 2000-2020 period performed with the two indices SPEI and SPI at 12-months timescale is reported in table 1.

Nine are the main episodes, and they are mainly summer events. Among them remarkable is the 12 July 2003 - 29 August 2003 episode characterised by a length of 8 consecutive weeks and 70% of northern Italy interested. Luterbacher et al., (2004) shows that this event is the result of a severe heatwave that affected not only northern Italy but also several Central European regions and the Mediterranean Basin. This event is driven by the positive phase of the East Atlantic teleconnection pattern that brought to positive temperature anomalies between the British Isles and Scandinavia (Baronetti et al., 2020). Table 1 shows also that, after this episode, droughts events become frequent and the most severe are in 2005 (1 May 2005 to 18 August 2005 ) with 25% of area interested and a duration of 12 consecutive weeks and 2017 (26 June 2017 to 29 August 2017) with 35% of extension and duration of 8 weeks. This intensification in the number of events is not localised only in Italy but interest the whole Mediterranean basin (Gudmundsson and Seneviratne, 2015). This is probably related to the North Atlantic Oscillation that has migrated to more northerly regions (200-300 hPa), generating positive temperature anomalies (Wallace & Gutzler, 1981).

Table 1: The main spring and summer drought episodes during the 2000–2020 period were analysed using 12-month SPEI and SPI indices. The table details each event, including its starting and ending week, duration (in weeks), and the percentage of the area affected by drought.

SPEI				SPI			
Start	End	Week	%Area	Start	End	Week	%Area
12/07/2003	29/08/2003	8	70	12/07/2003	29/08/2003	8	50
05/03/2004	06/04/2004	4	86	05/03/2004	22/04/2004	6	55
01/05/2005	18/08/2005	12	25	01/05/2005	28/07/2005	10	40
10/06/2006	26/06/2006	2	25	10/06/2006	26/06/2006	2	32
07/04/2007	23/04/2007	2	30	06/03/2007	09/05/2007	8	40
21/03/2012	06/04/2012	2	25	21/03/2012	06/04/2012	2	35
25/05/2014	10/06/2014	2	25	25/05/2014	10/06/2014	2	25
26/06/2017	29/08/2017	8	35	25/05/2017	29/08/2017	12	40
25/06/2020	28/08/2020	8	25	24/05/2020	11/07/2020	8	30

Table 1 has figured out a good agreement between drought episodes observed by the two indices, except for two events. The first, according to SPEI, goes from 7 April 2007 to 23 April 2007 (2 weeks) and interested 30% of the study area. Whereas, the SPI, detected a longer (6 March 2007 to 9 May 2007) and stronger event (40% of area under drought). Similar results are observed for the event in 2017, where the two indices detected the same ending week (29 August 2017) but the SPI identified a stronger (40% of area under drought) and a longer drought event with an earlier starting week (25 May 2017). This behavior is confirmed by the comparison between the percentage of area under drought estimated by the two indices (SPEI and SPI, Figure 4). Generally SPI used to define droughts episodes that are more spatially extended than SPEI (between 20% and 30% more), and this is observed for both severe and extreme episodes. This suggests that in the recent years the main drought

triggering factor is linked with the precipitation deficit. Baronetti et al. (2020) highlights that 2003 could be considered as a turning point in drought behavior, in fact before 2003 drought seems to be related to positive evapotranspiration anomalies while after, the main cause appeared to be the change of precipitation distribution. In fact, northern Italy, like several Mediterranean regions, is characterized by a high interannual variability of annual precipitation. This brought to no significant positive or negative precipitation trends for the last decades (Fratianni & Acquotta, 2017). On the other hand since the 2000s an increase in the duration of dry periods and more frequent and extreme precipitation events were observed by Acquotta et al. (2019) and Baronetti et al. (2018).

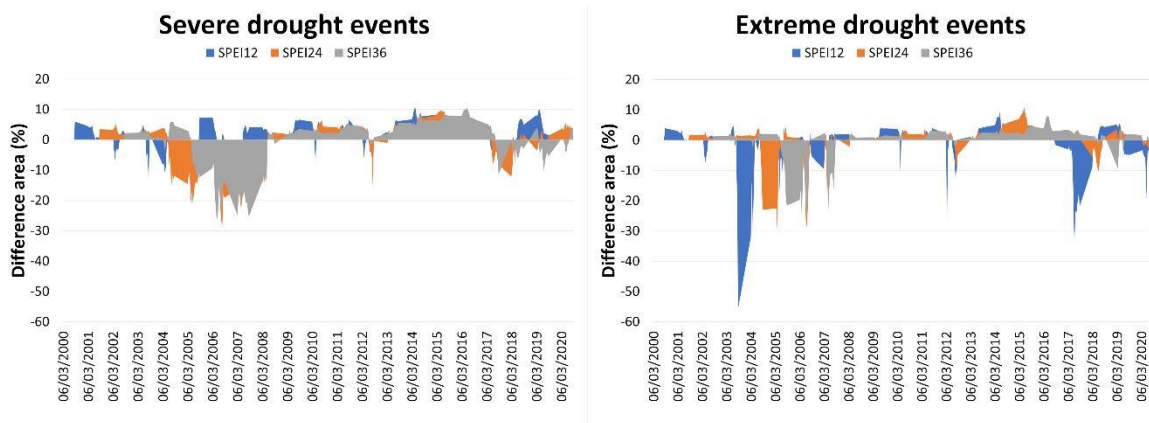


Figure 4: Differences in the percentage of area under between SPEI and SPI estimates are illustrated for drought severe and extreme drought conditions. Blue indicates the area difference between SPEI and SPI at a 12-month temporal aggregation scale, orange represents the 24-month scale, and gray corresponds to the 36-month scale.

The analysis on the spatial distribution of the main severe and extreme spring and summer drought events has resulted in the map reported in figure 5. The map has evidenced that the most interested areas are the Po Valley and the Tuscany hills partially. Here a maximum length of 4 consecutive weeks is detected for severe events and 2 weeks for extreme events. Long severe drought events of 2 and 3 consecutive weeks were also observed in the Occidental Alps.

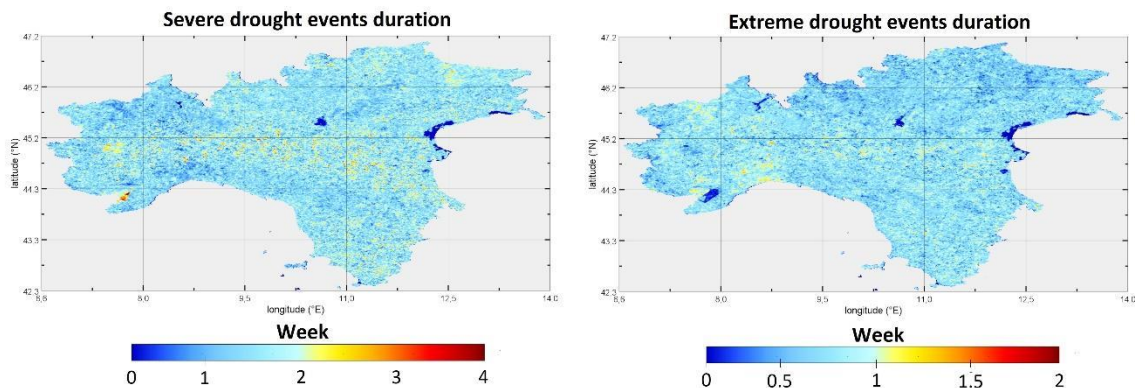


Figure 5: Spatial distribution of severe (left) and extreme (right) drought events length expressed in consecutive weeks.

These sectors are interested by a drought intensification (Figure 6), and the trend analysis performed on SPEI and SPI indices at 12-months shows negative and not significant

trends in the Occidental Alps (-1 and -2  $\Delta$ SPEI/year) and in the Tuscany hills (-1  $\Delta$ SPEI/year). While in the Po Valley SPEI trends are negative and significant (between -1 and -3  $\Delta$ SPEI/year). In the other sectors of the study area trends are close to zero except for the north-eastern Alps, where a decrease in drought severity was observed with positive and significant trends (1 and 2  $\Delta$ SPEI/year). These results partially contrast with what is observed for temperature in northern Italy. In fact Ceppi et al. (2012) figured out that the Alps has experienced the most intense and rapid temperature increase, and this trend will continue also for the next decades (Zimmermann et al., 2013 and Baronetti et al., 2022). This warming will intensify during the summer months (Gobiet et al., 2014), resulting in future glacier volume losses of approximately 80%–90% by the century's end (Radić et al., 2014) and in a decrease of permafrost thickness (Pogliotti et al., 2015).

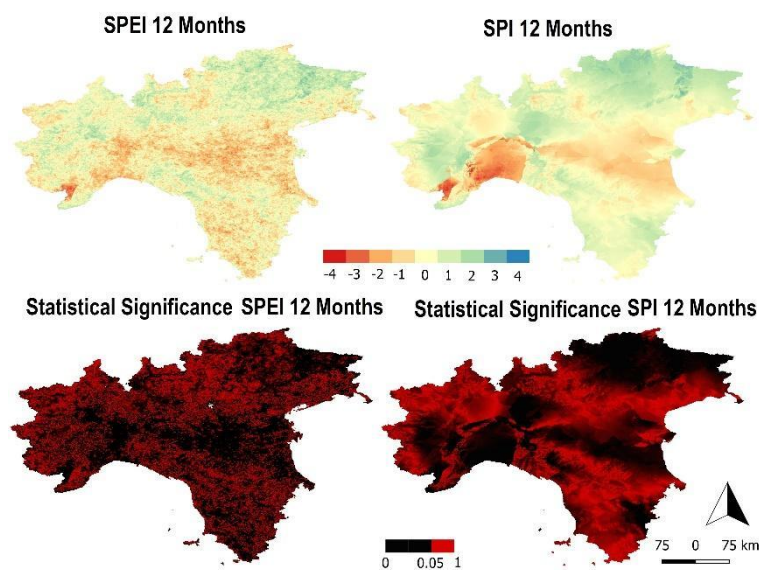


Figure 6: Drought trends calculated for SPEI and SPI at 12 months. In the upper panel the spatial distribution of the trends (red negative trend and blue positive trend) were showed, in the lower panel the statistical significance (black for p-value < 0.05)

### 2.1.3.2 Vegetation response to droughts

The investigation on drought effects on vegetation greenness started with the analysis of the bi-weekly vegetation indices (NDVI and EVI) trends (Figure 7). Keeping the results on droughts, the Po Valley and the Tuscany hills recorded negative and not statistically significant trends (NDVI trends between  $-0.10$  and  $-0.05$   $\Delta$ NDVI/year). While in few surrounding areas, positive NDVI trends of  $0.1 - 0.15$   $\Delta$ NDVI/year were observed. Figure 6 suggests a significant negative response to drought of Plain and Tuscany hills in summer and spring. This pattern is characteristic of the Mediterranean climate, where the significant increase in interannual variability during the growing season is well defined (Thiébaud and Moatti, 2018; Shafran-Nathan et al. 2013). Our findings indicate that drought episodes are likely to become more frequent in some temperate regions of northern Italy. Tardella et al., (2016) figured out that changes in the precipitation regime in this area are expected to impact the structure of natural grasslands, leading to forage quality deterioration. But also reduced

availability of grasslands for animal feeding (Scocco et al., 2016), and the development of a more fragmented vegetation mosaic (Chelli et al., 2016).

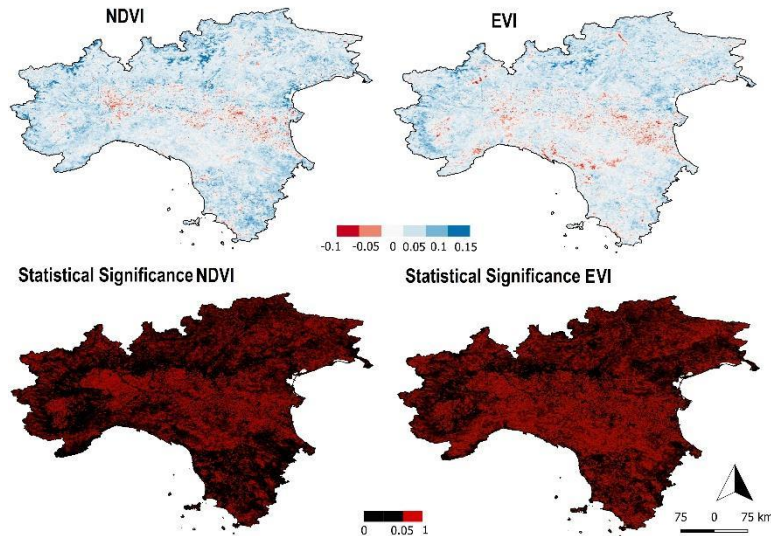


Figure 7: Vegetation trends calculated for NDVI and EVI vegetation indices. In the upper panel the spatial distribution of the trends (red negative trend and blue positive trend) were showed, in the lower panel the statistical significance (black for p-value < 0.05)

In detail the maps of the annual and seasonal investigation on water balance for drought and non-drought years is reported in figure 8. For drought years, a negative water balance between -900 and -500 mm was recorded in most of the study area except for the highest peaks of the Alps (positive values from 0 mm to 100 mm). For drought years an averaged water balance of -522 mm was observed for the entire study area. While for non-drought a less negative water balance was observed for the Po Valley and Tuscany hills and marked positive values were recorded along the mountain range (from 200 mm to 400 mm). The averaged water balance of -189 mm was observed for the entire study area. This highlights the traditional role of mountains as water sources, exhibiting a positive water balance. In contrast, the Po Plain is characterized by a negative local water balance, as it primarily relies on water availability (surface of ground) supplied by the surrounding mountains (Viviroli et al., 2007). Seasonally marked differences between drought and non-drought years were detected in spring (figure 8b). In fact, in non-drought conditions a negative water balance between -300 and -500 mm was limited only in the Po Valley and Tuscany hills, while for the surrounding areas positive values between 100 and 300 mm were observed. For drought years the Alps recorded negative water balance too (from -400 to -200 mm). This suggests a strong control of drought on vegetation during spring, and this is particularly marked in the Po Valley and Tuscany hills. The study figured out that the water balance in these areas during drought years is similar to that observed in southern Mediterranean regions such as Spain and Greece (Gouveia et al., 2017). On the other hand similar water balance rates for drought and non-drought years were identified in summer. Here from -500 to -300 mm of summer water balance was recorded in western Alps, the Po Plain, and the Tuscan hills (Figure 8c).

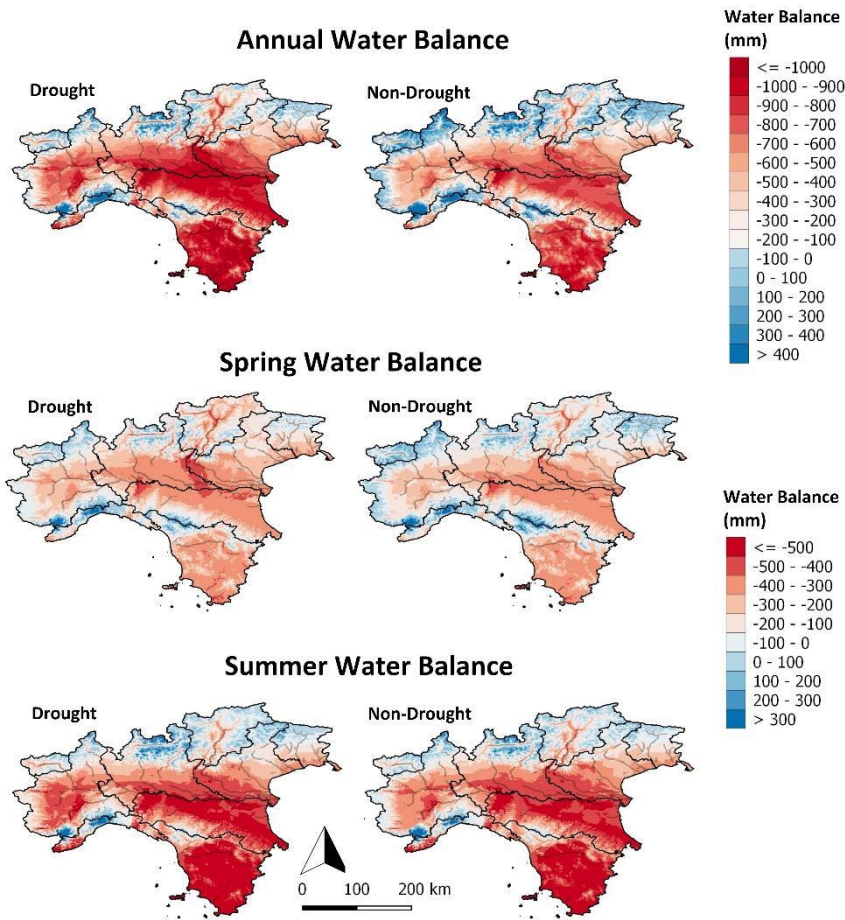


Figure 8: Spatial distribution of the water balance in northern Italy for three periods: the entire year (upper panels), spring (central panels) and summer (lower panels).

Once defining the link between drought and vegetation stress in the Po valley and Tuscany hills, maps that illustrate the summer and spring correlation between drought and vegetation were produced. In figure 9 and table 2 are reported the correlation between bi-weekly drought (SPEI and SPI) and bi-weekly vegetation (NDVI and EVI) indices at medium (12 months) and long (24 and 36 months) timescales. The strongest and statistically significant correlation were reached in the Plain and Tuscany hills for both the indices, and looking at the percentage of vegetation under drought it is clear an increase passing from medium to long timescales (Table 2). In fact, looking at the SPI index (which used to detect larger percentages instead of SPEI) at medium timescale detected 7% and 9% of vegetation under drought using the EVI and the NDVI index. At 36 months the percentages doubled and are 18% for NDVI and 13% for EVI.

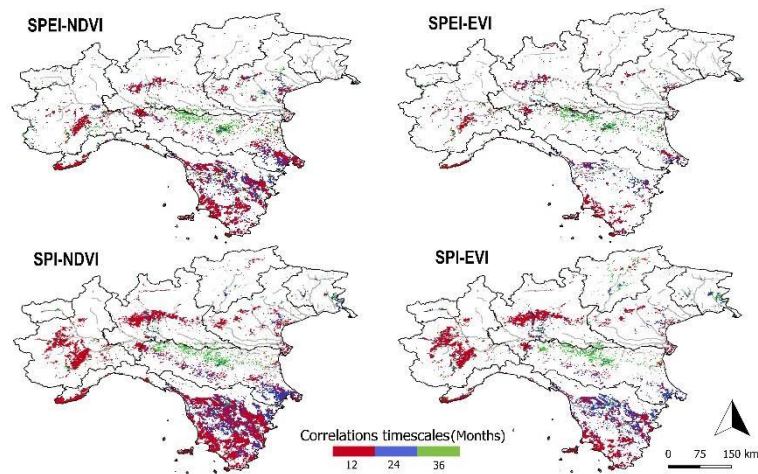


Figure 9: Aggregation timescales of SPEI and SPI with significant correlations to NDVI and EVI are presented. The color bar represents the aggregation timescale in months. Non-significant correlations ( $p\text{-value} \geq 0.05$ ) were excluded, and only the strongest Pearson correlation coefficients ( $r > 0.6$  or  $r < -0.6$ ) are shown.

Table 2: Percentage of total vegetation affected by drought, determined as the percentage of pixels showing significant and strong correlations between bi-weekly vegetation indices (NDVI and EVI) and drought indices (SPEI and SPI) at 12-month, 24- and 36-month timescales.

Timescale	Percentage of total vegetation (%)			
	SPEI-NDVI	SPEI-EVI	SPI-NDVI	SPI-EVI
12 Months	7	4	9	7
24 Months	9	5	13	9
36 Months	13	6	18	13

In table 3 are listed the main vegetation communities observed in northern Italy and the percentages of them under drought according to drought conditions at medium and long timescales. The results showed that the most sensitive class to drought with a percentage of 15.41% (SPI-NDVI) at 12 months and of 22.67% at long aggregation timescale (36 months) is the Natural Woody Wetlands. In the Mediterranean basin this is a heavily impacted community, experiencing a 50% loss over the past century (Geijzendorffer et al., 2016). Changes in land cover and in human population density significantly contributed to the fragmentation and the decline of this vegetation community (Bradshaw & Brook, 2014). These dynamics had severe effects, not only on wetlands but also on human well-being at both local and regional scales (Leberger et al., 2020).

Other two classes gave important percentages increasing at long drought timescales: forests and natural herbaceous located in rural sectors with intense human activities (Forest/Cropland Mosaics and Natural Herbaceous/Croplands Mosaics). Specifically the correlation between SPI and NDVI showed that at 12 months the 14.85% of herbaceous and the 26.75% of forest are under drought. While at 36 months the 26.85% of herbaceous and the 39.02% of forest were drought stress affected. This suggests that all the ecosystems (herbaceous or forest), constantly perturbed by human activities (cultivated areas), are more sensitive to drought. Since the mid-20th century, Italy, especially the Po Plain, has

experienced a rise in monoculture practices, primarily rice and corn cultivation. This shift has led to a decline in habitat biodiversity and increased fragmentation of natural areas (Cardarelli et al., 2011). Grossiord (2020) explains that in such stressed communities, species that share the same ecological niches have an intense competition for resources and often this reduces their resistance or resilience to drought. On the other hand, natural herbaceous communities with high biodiversity levels tend to be less impacted by droughts and recover more rapidly after these events (Isbell et al., 2015). Scocco et al. (2020) shows that in the Mediterranean basin plant communities respond to drought in various ways. Herbaceous species, in particular, have developed specific adaptation strategies to resist dry periods, such as annual lifecycle, maintaining overwintering leaf persistence, or utilizing storage organs (Galmés et al., 2007; Tardella & Catorci, 2015). In fact in our study the natural herbaceous class recorded lower percentages of vegetation stress and they are not increasing at longer timescales.

Similar results were observed for the natural forest classes too. For instance looking at Evergreen Needleleaf Forest the SPI-NDVI correlation shows a 7.46% at 12 months and a 8.40% at 36 months. Mediterranean forests, when not heavily disturbed, exhibit resilience to drought events, characterised by their ability to tolerate and recover from such conditions (von Keyserlingk et al., 2021). However, longer and severe drought periods during the typical wet season may increase the risk of forest fires, putting northern Italy's forests at significant risk (Turco et al., 2018; Vissio et al., 2023). Forest fires are particularly complex, and in the Mediterranean basin during the 2017 drought event, Italy, Greece, Portugal, and Spain experienced a total of 43,733 fires, which collectively affected 894,244 hectares (San-Miguel-Ayanz et al., 2018). For forest fire hazards, the spatial continuity of vegetation types plays a crucial role in Mediterranean ecosystems, influencing fire propagation and severity (Trucchia et al., 2023).

Table 3: Percentages of vegetation classes under drought, estimated on the percentage of pixels with strong and significant correlations between bi-weekly vegetation indices (NDVI and EVI) and drought indices (SPEI and SPI) at medium (12-month) and long (24- and 36-month) timescales.

	SPEI-NDVI (%)			SPEI-EVI (%)			SPI-NDVI (%)			SPI-EVI (%)		
	12	24	36	12	24	36	12	24	36	12	24	36
<b>Dense Forests</b>	3.22	3.27	3.62	1.22	1.26	1.35	4.82	5.78	5.49	2.50	3.04	3.32
<b>Evergreen Needleleaf Forests</b>	4.40	4.78	5.07	2.48	2.58	2.88	7.46	8.40	8.40	5.01	6.08	5.45
<b>Evergreen Broadleaf Forests</b>	5.34	4.96	5.47	3.05	3.68	3.25	8.47	11.13	10.00	5.81	7.50	8.97
<b>Deciduous Needleleaf Forests</b>	5.65	6.07	6.21	2.96	3.24	2.95	9.13	11.22	10.17	6.27	7.51	8.80
<b>Deciduous Broadleaf Forests</b>	6.09	6.24	6.98	1.93	2.82	3.12	9.05	11.73	9.84	5.96	7.06	9.06
<b>Broadleaf/Needleleaf Forests</b>	5.50	5.50	6.09	1.48	2.22	2.37	8.67	11.03	9.16	5.91	7.29	8.02
<b>Broadleaf Evergreen/Deciduous Forests</b>	5.32	6.18	7.04	2.29	3.44	3.59	8.38	11.11	10.53	5.07	7.41	8.95
<b>Open Forests</b>	11.36	13.58	14.64	3.70	3.84	5.30	20.08	28.59	22.02	10.00	17.99	20.97
<b>Sparce Forests</b>	11.29	12.18	13.40	4.97	4.81	6.87	10.34	10.16	11.02	11.42	12.44	11.05
<b>Forest /Cropland Mosaics</b>	20.87	25.28	31.80	9.41	10.50	13.95	26.57	32.05	39.02	17.02	26.84	33.30
<b>Woody Wetlands</b>	7.93	10.11	12.39	4.16	6.40	10.84	15.41	19.33	22.67	8.88	13.00	16.43
<b>Herbaceous</b>	5.16	6.71	7.01	2.68	3.49	3.49	7.86	8.73	9.35	5.17	6.96	7.94
<b>Natural Herbaceous / Croplands Mosaics</b>	5.20	8.20	12.62	3.53	4.91	9.08	14.85	18.48	26.82	10.03	15.66	19.68
<b>Herbaceous Croplands</b>	3.32	3.22	7.20	2.477	2.94	6.49	5.06	5.85	8.54	3.93	5.02	8.02

## 2.2 Unmanned Aerial Vehicle (UAV) for remote sensing

The Institute of Geosciences and Earth Resources (IGG) of CNR is a member and founder of the Additional Service REMOTE of the CNR Territorial Area in Pisa. The Service aims to design, implement, and manage remote sensing tools used for diagnostic and investigative purposes, enabling the collection of qualitative and quantitative information about the environment and objects located at fine scale. The Service operates over 30 multirotor drones, including models such as the DJI MATRICE 300 RTK with L1 (RGB/LIDAR) and P1 (RGB 42MP) sensors, the DJI P4 Multispectral, the DJI MAVIC 3 Thermal, and the DJI MAVIC 3 Multispectral.

It must be taken into consideration the challenge of accessing small monitoring areas, makes the “backpackable multirotor” drones (small and lightweight) more practical, at the cost of losing resolution, which can still be ensured with an appropriate choice of flight altitude. However, these drones are less suited for studies of highly distributed ecosystems due to their limited autonomy. In such cases, it is necessary to use drones with high endurance and greater capacity to map large areas within reasonable timeframes.

The solution to this type of requirement lies in fixed-wing systems, particularly V-TOL (Vertical Take-Off and Landing) systems, which are fixed-wing drones capable of vertical take-off and landing and transitioning into regular flight.

### 2.2.1 *Songbird 150 Specifications and flight performance:*

The SONGBIRD is a fixed-wing UAV (Unmanned Aerial Vehicle) with vertical takeoff and landing (VTOL) capability. It can be used to gather professional aerial imagery or other remote sensing data. Its modular design enables it to carry various payloads for surveying, mapping, security and surveillance, inspections, search and rescue and precision farming.

While the SONGBIRD has excellent horizontal flight properties, the VTOL feature reduces the risk of damage to the UAV and the payload at takeoff and landing. It also allows the SONGBIRD to be used in almost any location – no runway or other infrastructure is needed. It is designed to close the gap between costly full-size aircraft operations and simple multirotor drones which are easy to deploy but have very limited flight time and range.

Below are the main technical characteristics:

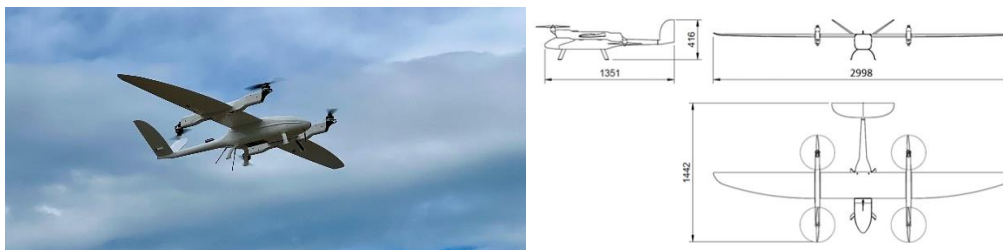


Figure 10: Singbird 150, Germandrones GmbH, Alt-Moabit 55 DE-10555 Berlin, germandrones.com, Songbird Manual version 3.2.2

Table 4: Dimensions, Speeds, Performance, Fly Time, Communications Set UP, Features and Transportation

<b>Dimensions:</b>	
<b>Span Width:</b>	2.98 m
<b>Length:</b>	1.44 m
<b>Body Material:</b>	GFRP, CFRP
<b>Empty Mass:</b>	7.6 kg
<b>Max. T/O Mass:</b>	14.0 kg
<b>Typical Load Examples:</b>	474 Wh (2.6 kg) Battery + up to 3.8 kg Payload or 622 Wh (3.2 kg) Battery + up to 3.2 kg Payload
<b>Speeds:</b>	
<b>Min Airspeed (AIRPLANE Mode):</b>	17.5 m/s (63 km/h)
<b>Max Airspeed:</b>	28.0 m/s (101 km/h)
<b>Cruise Airspeed:</b>	19.0 m/s (68 km/h)
<b>Wind (at Cruising-Altitude):</b>	max. 15 m/s (54 km/h)
<b>Wind (at Launch Site):</b>	max. 7 m/s (25 km/h)
<b>Performance Songbird 150:</b>	
<b>Propulsion:</b>	Four Electric Motors with tilt mechanism
<b>Installed Capacity:</b>	6.4 kW
<b>Power Consumption (Hovering):</b>	3 kW (at 11 kg TOM)
<b>Power Consumption (Cruise):</b>	450 W (at 11 kg TOM)
<b>Max Flight Time:</b>	
<b>474 Wh Bat. (8s Lipo 16000mAh), no Payload</b>	60 min
<b>622 Wh Bat. (8s Lipo 18000mAh), no Payload</b>	80 min
<b>474 Wh Bat. (8s Lipo 16000mAh), + Payload*</b>	50 min
<b>622 Wh Bat. (8s Lipo 18000mAh), + Payload*</b>	60 min
<b>Advanced Setup:</b>	
<b>Application &amp; Range:</b>	for BVLOS and/or live video operation, 5-10 km or up to 25 km with optional tracking antenna.
<b>RC (Backup Manual Control):</b>	433 MHz
<b>Telemetry &amp; Command:</b>	868 or 900 MHz
<b>Direct Video Link:</b>	2.4 GHz
<b>Features:</b>	
<b>Autopilot:</b>	Capable of Fully Automatic Missions, Auto Takeoff and Landing
<b>Safety features:</b>	Automatic Return to Launch, Self-Stabilization Geofencing
<b>VTOL capability:</b>	Yes
<b>Operating Temperature:</b>	-10 °C to 40 °C (preheat batteries to > 20 °C)
<b>Operator Training:</b>	Courses and Training Box (SONGBIRD operation in simulated environment) available
<b>Transportation:</b>	
Transport box:	120 cm x 60 cm x 38 cm

Set up time:	< 10 min
Tool-free Assembly	Yes

\*Payload example: Colibri camera + long range transmitter, powered by the flight battery

### 2.2.1.1 Part & Fixing:

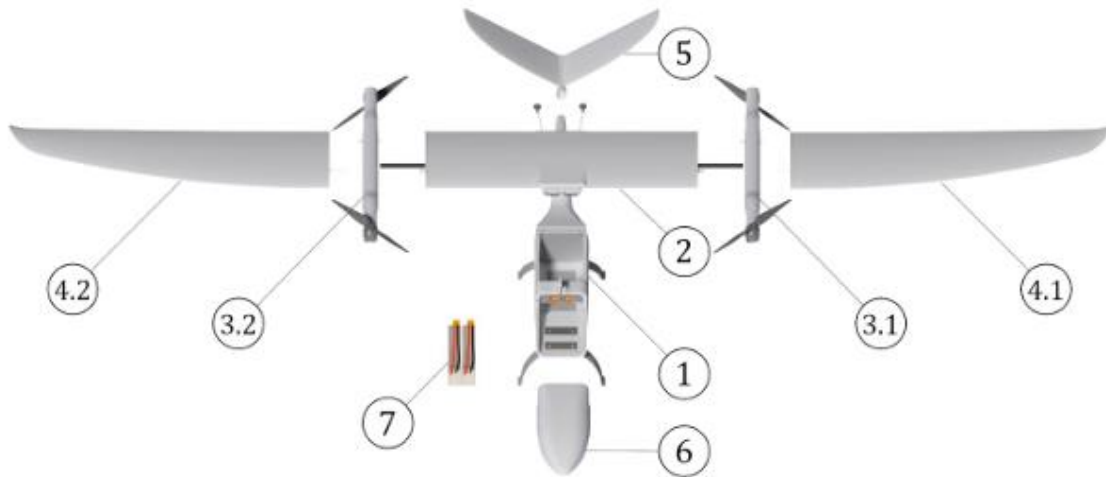


Figure 11: spare part drawing of the Singbird 150, Germandrones GmbH, Alt-Moabit 55 DE-10555 Berlin, germandrones.com, Songbird Manual version 3.2.2

Table 5: Part description

<b>SONGBIRD - AIRFRAME</b>	
<b>1</b>	Fuselage
<b>2</b>	Wing – Middle Section with Knurled Screws
<b>3.1</b>	Motor Arm Left
<b>3.2</b>	Motor Arm Right
<b>4.1</b>	Wing – Outer Section Left
<b>4.2</b>	Wing – Outer Section Right
<b>5</b>	V-Tail
<b>6</b>	Nose
<b>7</b>	Battery Pack (incl.sled)

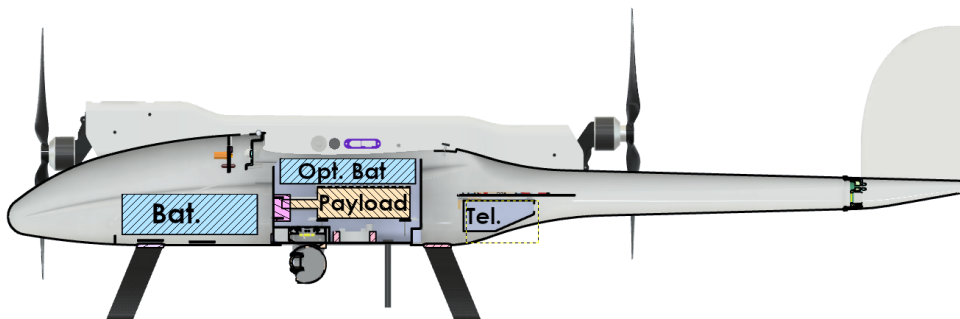


Figure 12: Section drawing of the Singbird 150, Germandrones GmbH, Alt-Moabit 55 DE-10555 Berlin, germandrones.com, Songbird Manual version 3.2.2

### 2.2.1.2 Radio Controlled (RC)

In figure 13 there are the position and function of the individual sticks for command and control of the drone.

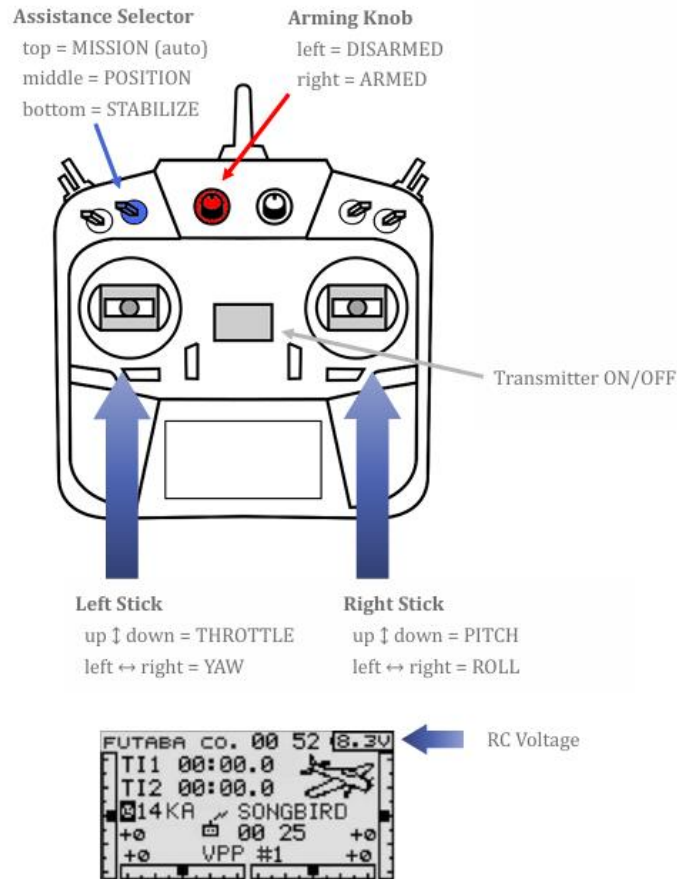


Figure 13: Radio control stick of the Singbird 150, Germandrones GmbH, Alt-Moabit 55 DE-10555 Berlin, germandrones.com, Songbird Manual version 3.2.2

### 2.2.1.3 Allowable Load

The maximum aircraft weight is dictated by the motors' ability to generate sufficient thrust for vertical flight under any given conditions. This is primarily influenced by the altitude above sea level and the air temperature.

The following figure refer to the location of takeoff and landing (COPTER mode). The conditions encountered during AIRPLANE-mode-flight are not decisive in this matter. The table specify the maximum load, which is the combination of payload and battery (Figure 14).

	< 0	0-5	5-10	10-15	15-20	20-25	25-30	30-35	35-40 °C
100	6,4	6,4	6,4	6,4	6,4	6,4	6,2	6,0	5,7
250	6,4	6,4	6,4	6,4	6,4	6,3	6,0	5,8	5,6
500	6,4	6,4	6,4	6,4	6,2	6,0	5,8	5,6	5,3
750	6,4	6,4	6,4	6,2	6,0	5,7	5,5	5,3	5,1
1000	6,4	6,4	6,2	5,9	5,7	5,5	5,3	5,1	4,8
1250	6,4	6,1	5,9	5,7	5,4	5,2	5,0	4,8	4,6
1500	6,1	5,9	5,6	5,4	5,2	5,0	4,8	4,6	4,4
1750	5,8	5,6	5,4	5,1	4,9	4,7	4,5	4,3	4,1
2000	5,6	5,3	5,1	4,9	4,7	4,5	4,3	4,1	3,9
2250	5,3	5,1	4,8	4,6	4,4	4,2	4,0	3,8	3,6
2500	5,0	4,8	4,6	4,4	4,2	4,0	3,8	3,6	3,4
2750	4,7	4,5	4,3	4,1	3,9	3,7	3,5	3,3	3,2
3000	4,5	4,3	4,1	3,8	3,7	3,5	3,3	3,1	2,9

*m MSL*

Figure 14: Max Load in Kg. – Fild elevation vs. temperature, Germandrones GmbH, Alt-Moabit 55 DE-10555 Berlin, germandrones.com, Songbird Manual version 3.2.2

### 2.2.1.4 Centre of Mass

To ensure stable flight characteristics, the center of mass must be positioned between 83 mm and 108 mm from the leading edge of the center wing (Figure 15). This requirement is fulfilled for all standard SONGBIRD configurations, including battery and payload combinations provided by Germandrones, and is verified for every setup delivered to customers. If it is suspected that this may have changed due to modifications, repairs, or other factors, please recheck the position of the center of mass.

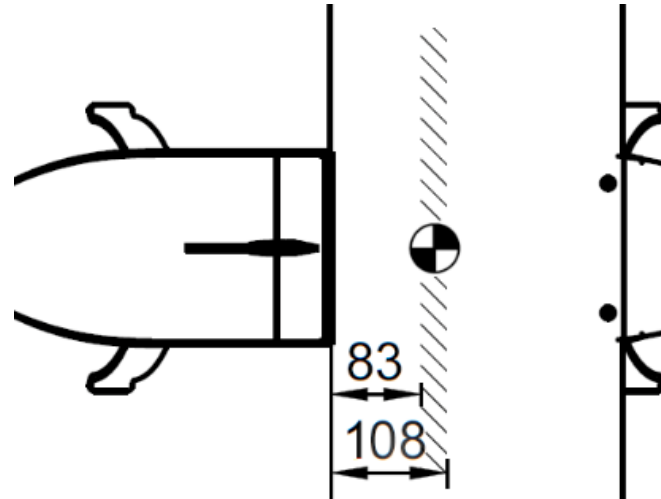


Figure 15: Centre of mas, Germandrones GmbH, Alt-Moabit 55 DE-10555 Berlin, germandrones.com, Songbird Manual version 3.2.2

The following image provide an indication of what flight time and distance can be achieved with certain setups.

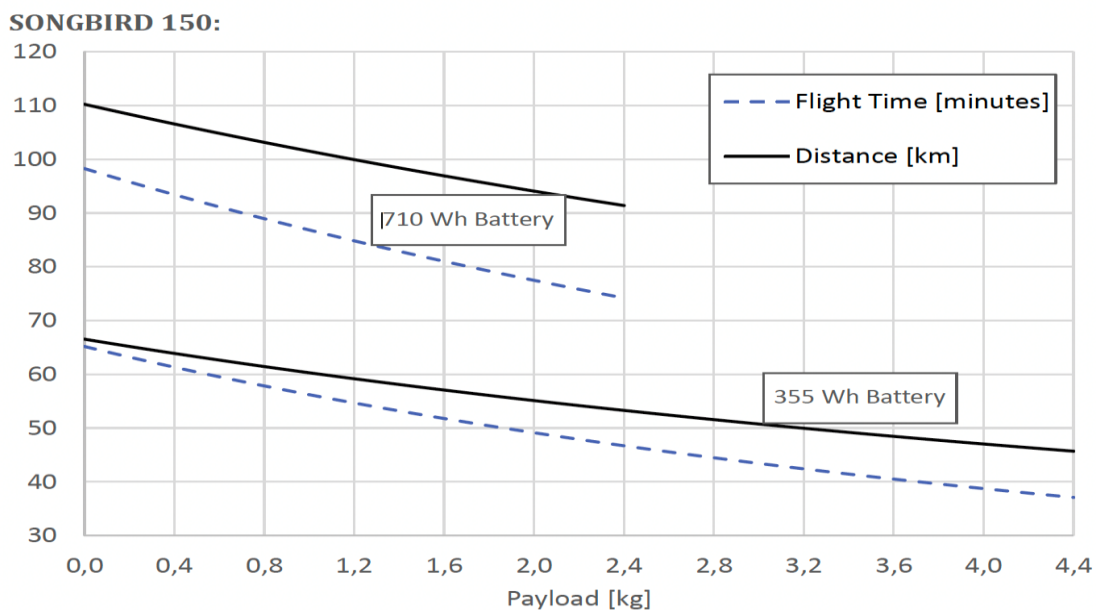


Figure 16: Flight time [min] e Distance [km], Germandrones GmbH, Alt-Moabit 55 DE-10555 Berlin, germandrones.com, Songbird Manual version 3.2.2

The data described in Figure 16 are originate from multiple flights in different conditions and represent an average. The performance depends on a variety of factors:

- Wind: can significantly decrease the distance over ground.
- Environmental factors: air density and temperature can impact the performance. Moreover, it is normal to see the power consumption change vividly as the flight controller reacts to thermals or turbulences. Therefore, the cumulative energy consumption can vary even between similar flights.
- Sources of drag: the gimbal camera payload and antennas. Any additional aerodynamic drag decreases the performance.
- The data do not include the additional power that some payloads draw from the flight battery. E.g. a long-range HD video transmitter can draw up to 45 W and thus decrease the flight time and range by up to 12 %.

### *2.2.1.5 Air Speed*

The default speed is 18-20 m/s. Since the flight controller cannot know the load of the UAV, the user must manually set an appropriate speed. It is recommended to use the table values in the user manual. It is not necessary to adjust it when flying lighter, i.e. a higher speed than specified in the table is fine but will be less economical. The default speed can be set on the flight software. Please note that this will only affect the speed temporarily - it will be reset when you change the flight mode. This option can be useful for quickly adapting the speed to changing conditions, when rain or strong winds arise.

### *2.2.1.6 Wind*

For safety reasons, the airspeed in COPTER mode and in and POSITION or MISSION mode is limited. If wind gusts exceed 6 m/s (21 km/h, please measured approximately 2 m above ground in an open area), the UAV may drift downwind or exhibit jerking movements, as the flight controller may struggle to compensate for the wind consistently. In such conditions, manual control may be necessary. In COPTER mode, wind speeds up to 10 m/s (36 km/h) can be managed in STABILIZE mode. In such conditions it is important to keep the Nose pointed towards the wind. While the wind speed at high altitudes is stronger (Figure 17) the SONGBIRD flies faster in AIR-PLANE mode, allowing it to handle winds up to 14 m/s (50 km/h) at cruising altitude.

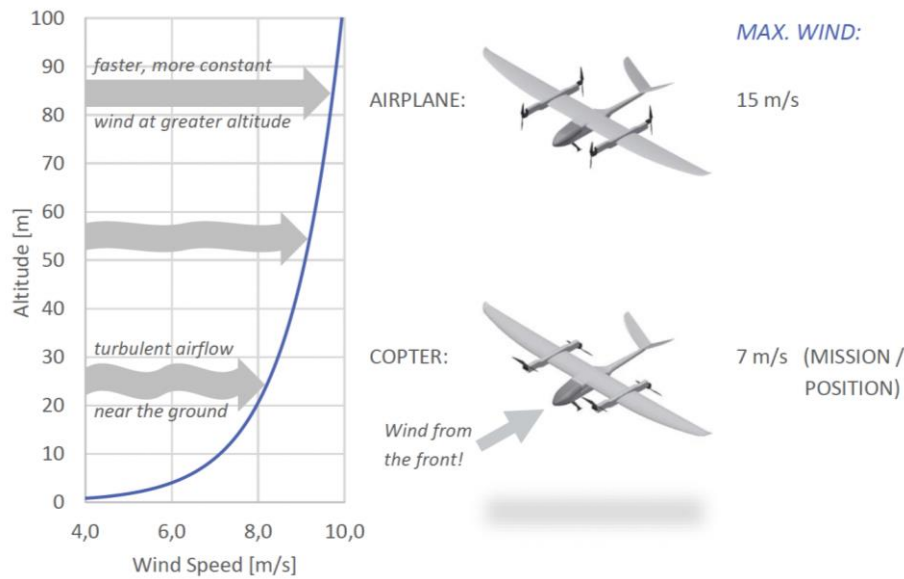


Figure 17: Wind Speed vs Altitudine, Germandrones GmbH, Alt-Moabit 55 DE-10555 Berlin, germandrones.com, Songbird Manual version 3.2.2

### 2.2.1.7 Rain

The SONGBIRD is splashing water resistant and can withstand moderate rain. However, prolonged exposure to wet conditions may reduce the overall product lifetime. It is recommended to interrupt the mission and conduct a normal landing if there is more than just a temporary drizzle. Rain can decrease lift and efficiency, if flight must continue increase the airspeed by at least 0.5 m/s to compensate.

### 2.2.1.8 Return & Landing Calculation

Batteries do not degrade linearly which can be critical for landings: right before they are fully depleted, their power drops to levels that can no longer support hovering or maintaining altitude. Therefore, the weights specified in table 6 Operating below this level may damage the batteries and compromise safe flight.

It is strongly recommended to initiate the landing approach when the battery status reaches 20% charge. Under certain conditions, additional margin should be added, as shown in the table 6.

Table 6: Minimum Battery Status (%)

<i>CONDITIONS</i>	<i>BEGIN LANDING APPROACH</i>	<i>LANDED</i>
Normal	20 %	10 %
Wind gusts 6 m/s (21 km/h) or more	add 5	add 5 %
Heavy load	add 5 %	add 5 %
Extended landing phase	add accordingly	

**Example:** With a fully loaded SONGBIRD the landing approach in windy conditions should begin at 20% + 5% + 5% = 30% battery level.

As a reference, a typical SONGBIRD consumes 1-2 % battery per minute or per kilometer in cruise flight. Should also refer to the “Battery Remaining” indication, which can be found in the Telemetry widget. It displays the remaining flight time based on the previous power consumption. An indication of “00:00” means the battery has just enough charge left for a transition to COPTER and a landing (from a maximum altitude of 50 m max.). Must be considered that headwinds can significantly reduce the actual remaining range.

Moreover the battery percentage indicator may be inaccurate if the wrong battery type is selected or if the battery wasn't fully charged. It is important always monitor the discharged mAh and the voltage for a more accurate assessment. While voltage is subject to various influences, as a general rule of thumb:

100% ~ 33.5V 30% ~ 29.7 V

50% ~ 30.1 V 20% ~ 29.4 V

#### *2.2.1.9 Fog or Clouds*

Flying in foggy conditions causes an accumulation of water on the aircraft's surfaces, similar to light rain. Such conditions should be treated with the same precautions as rainy weather.

### 2.2.2 Songbird 150 Sensor

The drone is equipped with a technical compartment specifically designed to house the PAYLOAD BOX. This BOX (Figure 18) is intended for the installation of sensors used to collect data during flight. Generally, it can accommodate RGB sensors, thermal cameras, multispectral sensors, and even LIDAR systems.

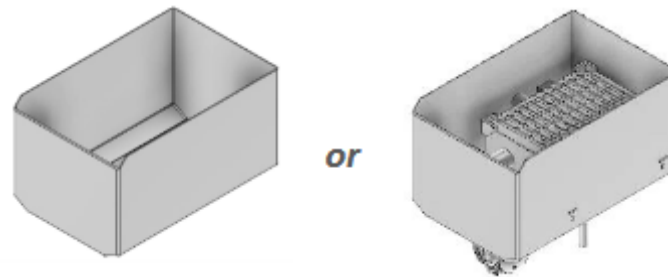


Figure 18: Payload box, Germandrones GmbH, Alt-Moabit 55 DE-10555 Berlin, germandrones.com, Songbird Manual version 3.2.2

In this specific configuration, two different devices have been selected: the PHASE ONE iXM 100MP and the Micasense Altium-PT (Figure 19).



Figure 19: PHASEONE iXM and Micasense Altium-PT

The first device is equipped with a 100MP RGB sensor and a mechanical shutter capable of capturing 3 images per second, making it particularly suitable for fixed-wing drones where cruise speeds are significantly higher than those of multirotor drones.

The second device is a multiparametric system featuring:

- 6 different channels at 3.2MP each (Red, Green, Red Edge, NIR),
- 1 Panchromatic channel at 12MP, and
- 1 thermal channel with a resolution of 320x256.

	Multispectral	Panchromatic	Thermal
Pixel size	3.45 $\mu\text{m}$	3.45 $\mu\text{m}$	12 $\mu\text{m}$
Resolution	2064 x 1544 (3.2 MP per multispectral band)	4112 x 3008 (12 MP panchromatic band)	320 x 256
Aspect ratio	4 : 3	6 : 5	5 : 4
Sensor size	7.12 x 5.33 mm (8.9 mm diagonal)	14.18 x 10.37 mm (17.6 mm diagonal)	3.84 x 3.07 mm (4.9 mm diagonal)
Focal length	8 mm	16.3 mm	4.5 mm
Field of view	48° HFOV x 36.8° VFOV (Multispectral bands)	46° HFOV x 35° VFOV (Panchromatic band)	48° HFOV x 39° VFOV (Thermal band)
Thermal sensitivity	n/a	n/a	< 60 mK
Thermal accuracy	n/a	n/a	+/- 5 K
Output bit depth	12-bit	12-bit	16-bit
GSD @ 120 m (394 ft)	5.28 cm/pixel per multispectral band	2.49 cm/pixel for panchromatic band and pan-sharpened multispectral bands	33.5 cm/pixel
GSD @ 60 m (197 ft)	2.64 cm/pixel per multispectral band	1.24 cm/pixel for panchromatic band and pan-sharpened multispectral bands	16.75 cm/pixel

Figure 20: Technical specifications Micasense Altium-PT

### Technical Specifications

	iXM-100	iXM-100 Achromatic	iXM-50
Resolution	100MP 11664 x 8750		50MP 8280 x 6208
Dynamic range (dB)	83		84
Aspect ratio	4:3		
Pixel size ( $\mu\text{m}$ )	3.76		5.3
Effective sensor size (mm)	43.9 x 32.9		
Light sensitivity (ISO)	50 - 6400	200 - 25600	100 - 6400
Capture rate (fps)	3		2
Camera type	Medium-format camera for aerial imaging		
Lens mount	Phase One RSM		
Data interfaces	USB3, Ethernet 10G		
I/O interfaces	Trigger, Mid exposure, Ready, Serial		
HDMI	1920 x 1080 60p		
Data storage	XQD card		
Synchronization speed	50 microseconds in an array of cameras		
Raw file compression 14bit	IIQ large: 100MB IIQ small: 65MB		IIQ large: 50MB IIQ small: 33MB
IR cut-off filter	Yes		
Connection to pod	4 x M4 bolts		
Power input	12 - 30 VDC		
Max. power consumption (w)	16		14
Weight - excluding lens (g)	630		
Weight - including 80mm lens (g)	1100		
Dimensions - excluding lens (mm)	90 x 90 x 68		
Dimensions - including 80mm lens (mm)	90 x 90 x 164		
Approvals	FCC Class A, CE, RoHS		
Temperature ( $^{\circ}\text{C}$ )	-10 to 40		
Humidity (%)	15 - 80 (non-condensing)		

Figure 21: Technical specifications PHASEONE iXM

The flight plan must be tailored to the type of instrumentation onboard. To generate radiometrically and geometrically accurate orthophotos, it is necessary to apply overlap between individual frames. The overlap must be both frontal and lateral, and it should never fall below 60%; typically, an overlap of 70%-75% is used.

These parameters depend not only on the sensor but also on the type of flight operation (e.g., corridor mapping or area mapping), the altitude, and the terrain morphology. The correct parameters can be determined using flight planning software and the simulator BOX, which allows flight testing during the planning phase.

## 2.2.3 Songbird 150 Ground Control Station and Mission Planning

### 2.2.3.1 Ground Control Station (GCS)

The Germandrones VTOL SongBird 150 flight system provides a dedicated command and control software called "DroneIntelligence", designed for Windows (Figure 22).



Figure 22: Main screen DroneIntelligence

The “Drone Intelligence” software enables mission planning, simulation, and real-time drone management during both standard operations and emergencies. During the flight, users can monitor nearby air traffic, track data acquisition progress, and view telemetry details such as absolute speed, altitude, wind conditions, estimated temperature, position, battery level, and more. From the same interface it is possible to send specific flight commands and adopt possible emergency actions such as:

- HOLD: Set up an immediate circular flight.

- LOITER Directs the UAV to circle a specified point while awaiting further instructions.
- RTH (Return to Home): Commands the UAV to return to its designated home position.

In emergency scenarios, it is advisable to pre-plan potential reentry routes; based on the terrain and obstacles not covered by the initial flight plan. This helps prevent collisions with unaccounted structures.

### 2.2.3.2 *Transitioning*

The SONGBIRD 150 is equipped with powerful motors, making it suitable for carrying heavier payloads and operating at higher altitudes. Although this results in higher power consumption, additional batteries can be accommodated in the payload compartment to extend operational time.



Figure 23: Copter configuration



Figure 24: Plane configuration

The flight controller facilitates smooth transitioning between the COPTER mode (Figure 23) and AIRPLANE mode (Figure 24). The COPTER mode is only adopted for takeoff and landing. Prolonged hovering in COPTER mode is discouraged, as it significantly reduces flight time. During a mission, the SONGBIRD can loiter over a point of interest in AIRPLANE mode.

The transition altitude is determined by the altitude of the previous waypoint, which the UAV maintains until initiating its vertical descent to hover over the designated landing waypoint. The altitude profile of a typical landing approach is illustrated in Figure 25.

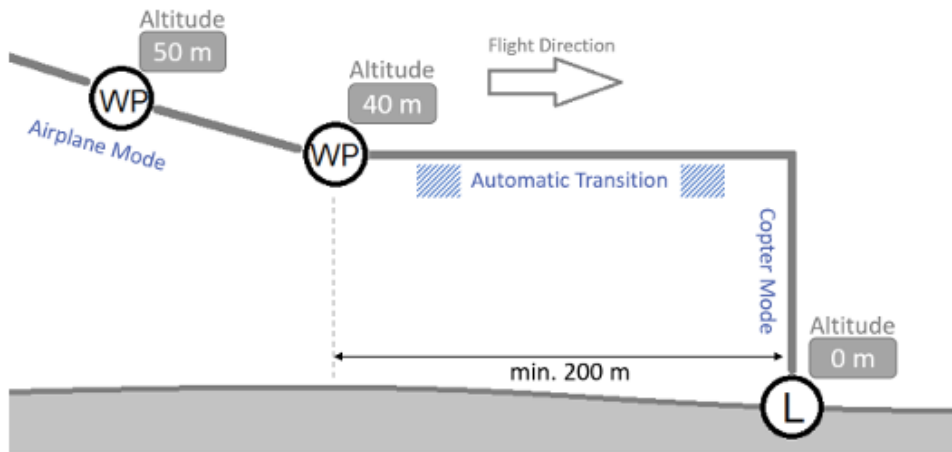


Figure 25: Altitude profile of a typical landing approach

### 2.2.3.3 Simulator

The GCS flight planning software includes also a simulator that can replace the SongBird 150 for testing purposes (Figure 26). This option allows the user to verify the feasibility and robustness of the entire mission; Once activated, the user can interact with the system through both the GCS interface and the portable radio control unit.



Figure 26: PC and simulation box

### 2.2.3.4 Terrain Follow function

The Elevation Plot profile is used to revise the planned mission altitude (Figure 27). The red solid line displays the averaged landscape relief (based on SRTM - Shuttle Radar Topography Mission data retrieved online), while the green line shows the navigation waypoints. It is important to note that the SRTM data has limited resolution and do not include obstacles like buildings, trees, power poles and more.

The plot horizontal axis displays the travel distance (in meters) and the vertical axis shows the altitude above Mean Sea Level (MSL) in meters.

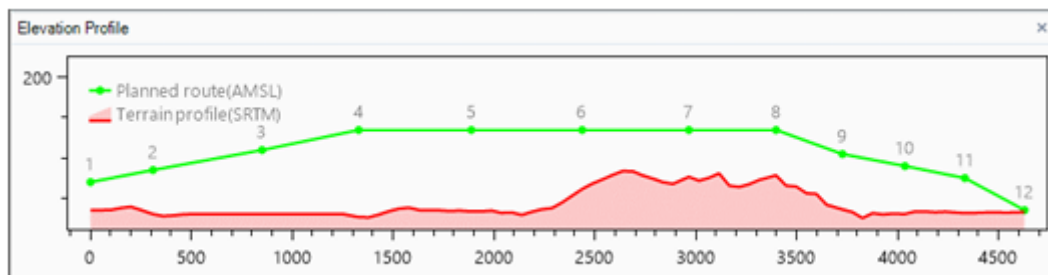


Figure 27: Elevation Profile

The objective of the “follow” function is to generate a flight plan at a constant altitude relative to the ground and not relative to the MSL. This working mode guarantees a constant resolution of the output obtained.

## 2.2.4 Songbird 150 Functions

### 2.2.4.1 Area scan (Survey)

The flight path for an area scan is created (Figure 28) within a defined polygon, based on a variety of parameters editable in the corresponding entry in the Waypoints widget. These parameters include altitude, angle, and the distance between flight lines. The trigger distance determines how frequently a camera trigger signal is sent to the payload. Additionally, the user can set a turn-around distance to make the UAV fly beyond the polygon border before turning around.



Figure 28: Area scan mode

#### 2.2.4.2 Corridor

The Corridor tool offers similar set of parameters to the Survey function but is designed for line-based missions. Instead of scanning an area, it follows a specified line with lateral offsets for each pass, making it ideal for corridor mapping (Figure 29).



Figure 29: Corridor scan mode

#### 2.2.4.3 Loiter

Loiter waypoints are optional and allow the UAV to circle a specified location (Figure 30). In the Waypoints widget, the user can set the altitude and the duration (in seconds) before the UAV moves to next waypoint, and the loiter radius, which can be adjusted either in the list or directly on the map by dragging the handle of the loiter circle.

For advanced users, selecting the “Loiter 8 shape” checkbox (Figure 30) enables the UAV to follow a figure-eight-pattern instead of a circle. In this case it is recommended to set the radius to at least 200 m to ensure a proper flight path.

Loiter functions is especially useful for altitude adjustments and emergency management.

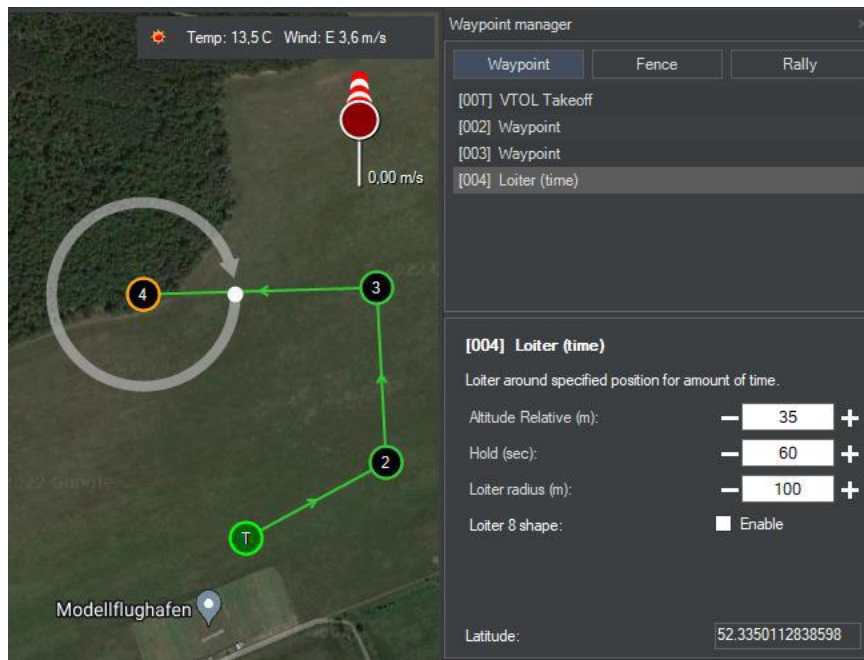


Figure 30: Loiter set-up page

#### 2.2.4.4 HOLD (Emergency Action)

During a mission, activating the HOLD function will make the UAV start loitering (circling) around its current position at the same altitude. The loiter radius can be adjusted via a button that appears in the bottom-right corner of the map.

### 2.2.5 Songbird 150 Head-up Display and Telemetry

This element visualizes the UAV's orientation in space. It combines several basic instruments to display the pitch and roll angles as well as the airspeed (left bar graph) and relative altitude (right bar graph). It also includes a compass at the bottom. Flight Time, GPS Status and Battery percentage are always shown at the top of the artificial horizon widget (Figure 31).

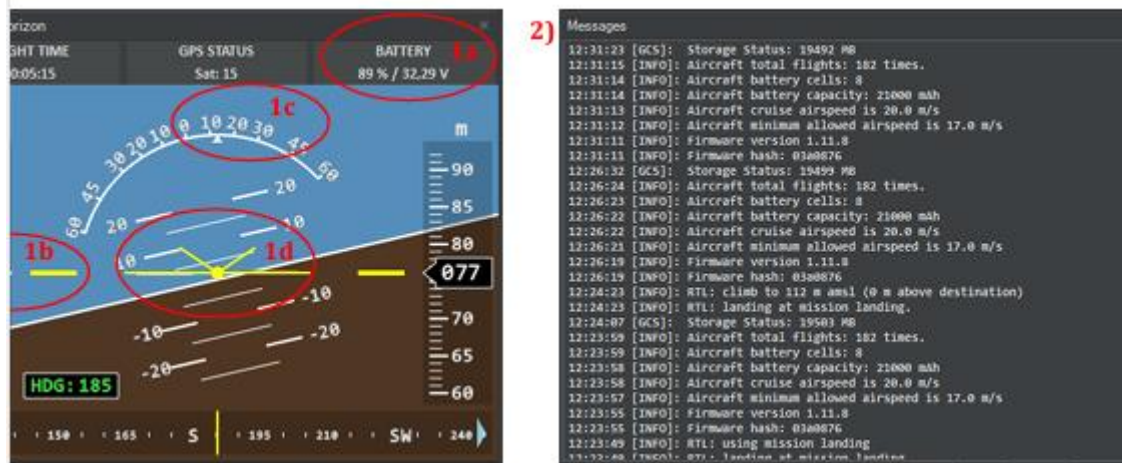


Figure 31: Head-up display example

#### 2.2.5.1 Battery Plot

The Battery Plot is accessible from the View menu, and it compares the expected voltage of the flight battery to its actual value (Figure 32). A noticeable drop in the orange plot compared to the green plot indicates reduced battery performance. Reduced battery performance can be associated with low temperature (which improves as the battery warms) or poor battery health. A strong and persistent deviations can indicate a loss of usable capacity; in such cases, allow for an extra safety buffer and replace the battery soon.

**Note:** To ensure the Battery Plot functions correctly, the correct battery type must be selected. Right-click the battery percentage indicator to verify or adjust the selection.

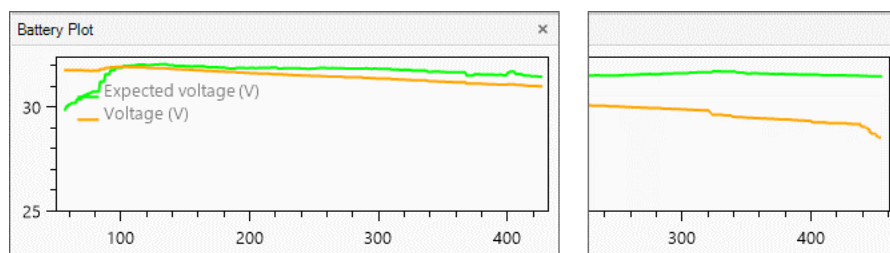


Figure 32: Head-up display example

#### 2.2.5.2 Wind Indicators

When connected to the internet, weather conditions for the current map location are displayed in the upper-right corner of the map (Figure 33).

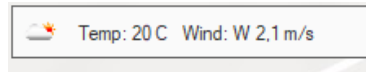


Figure 33: Temperature and Wind for the current map location

The flight controller calculates the wind direction and speed by comparing differences between air- and groundspeed. This data may be imprecise until the SONGBIRD has been cruising for some time. The wind is visualized with a windsock symbol on the map (Figure 34):

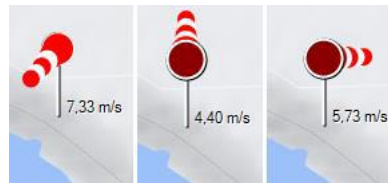


Figure 34: Wind for the current map location

- Example: 7.3 m/s from the northeast, 4.4 m/s from the south, or 5.7 m/s from the west.

This information is also available in the Telemetry widget and is used during automatic landings to orient the UAV's nose into the wind for optimal performance.

### 2.2.6 Songbird 150 Assembly:

- 1) **Install the Payload Box:** Begin by placing the payload box inside the fuselage. For training purposes, an empty box can also be used;
- 2) **Connect the Telemetry Module:** Connect the Telemetry Module to the ground control station (GCS), then start the GCS;
- 3) **Attach the Middle Wing Section (Figure 35):** Place the middle section of the wing on the fuselage and push it forward to connect the plugs. Secure it by tightening the two knurled screws;



Figure 35: Middle section

- 4) **Attach the Motor Arms (Figure 36):** Slide the motor arms onto the carbon tubes of the middle wing and connect the plug. Align the small anti-torsion pins of the arms with the corresponding holes in the middle section of the wing. Repeat this for the other side. Be cautious, as the UAV may tip over if only one arm is attached;



Figure 36: Motor arm

- 5) **Install the Outer Wings (Figure 37):** Attach the outer wings by connecting them in the motor arms in the same manner. Once pushed into place, the locking mechanism will hold both the wings and the motor arms.



Figure 37: External wing

6) Attach the V-Tail (Figure 38): Plug the v-tail boom and secure it using the knurled screw at the back of the v-tail. Ensure that the v-tail securely fixed without any play after tightening the screw.



Figure 38: V-Tail

7) Install the Battery Sled: Place the battery sled on the rails inside the fuselage. Slide it forward until it locks with a “Click” inside the locking mechanism. Tighten the Velcro straps to secure the battery. For safety and energy conservation, it is recommended to connect the battery just before flight. Always ensure the propellers are clear, and never arm the motors while people are near the UAV. Connect both yellow connectors, ensuring they are tightly fitted.

8) Attach the Nose (Figure 39): Attach the nose by pushing the plastic knobs of the nose into the designated cavities in the fuselage.

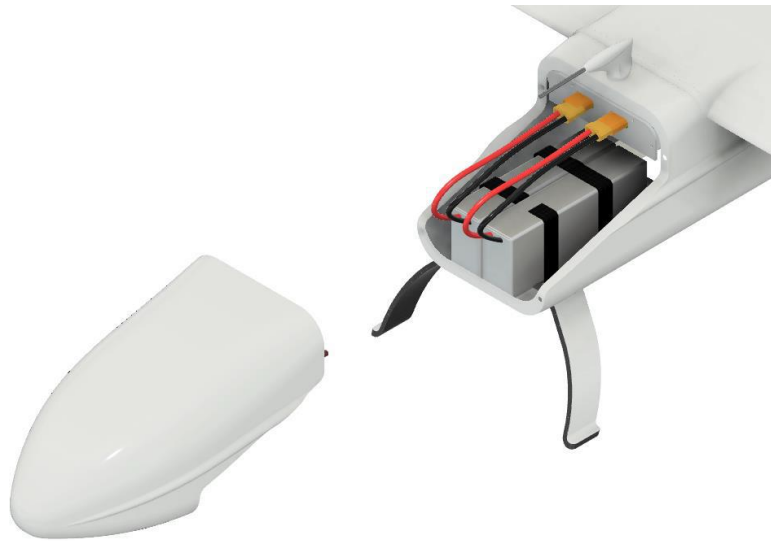


Figure 39: Nose

### 2.2.7 Songbird 150 ADS-B System

The Songbird 150 is equipped with advanced surveillance technology that combines the aircraft's positioning system, avionics, and ground infrastructure to provide accurate surveillance between the aircraft and air traffic control (ATC). The ADS-B GCS function (Figure 40) displays other aircraft in the map when using the optional ADS-B receiver, which connects to the GCS via USB.

In this case we use PingUsb Uavionix receiver.

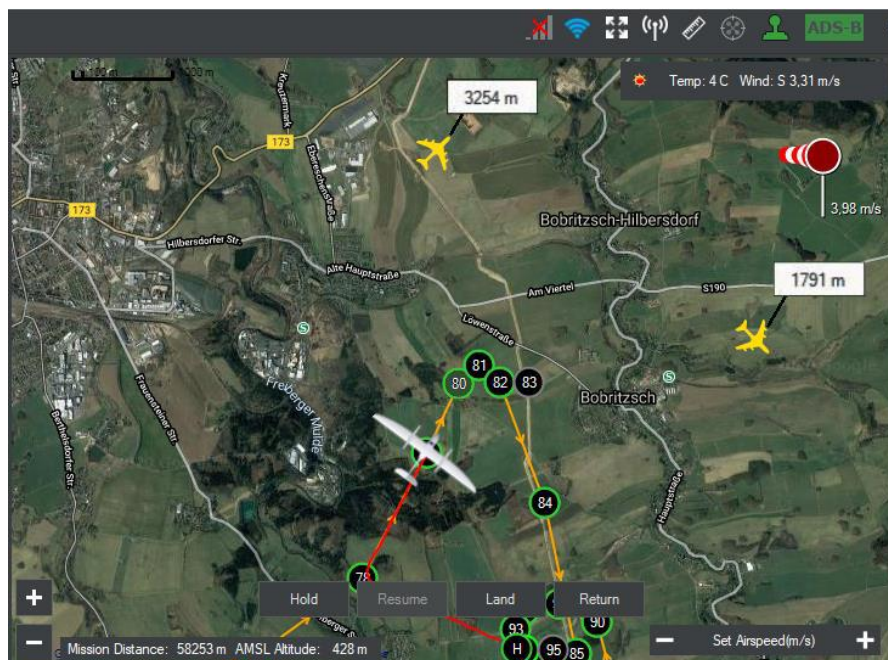


Figure 40: Other planes on the map

The Songbird is equipped with an ADS-B transmitter. It can transmit its telemetry and its identification code in real time. This feature is currently inactive, and the process of obtaining the unique ICAO code (or hex code) is ongoing.

### 2.2.8 Mobile Research Unit

The drone command and the control system, with the aid of the remote controller (described in section 2.2.1.2), manages automatic flight modes and manual flight phases when necessary. Additionally, using the GCS (described in section 2.2.3), it oversees all automatic functions preloaded into the planning algorithm.

The SongBird is operated by two pilots: a primary pilot (PIC - Pilot in Command, Figure 41) who uses the remote controller and monitors flight phases visually, and one (or more) secondary pilot who handle the drone telemetry (Figure 42) and execute actions based on the PIC's instructions.

Therefore, the ground maneuvering area, which includes takeoff and landing zones and areas for equipment management as shown in Figure 43, accommodates both the PIC and the co-pilot. The main difference is that the PIC performs maneuvers with the drone in sight, while the co-pilot supports the PIC by issuing commands in non-visual mode.



Figure 41: PIC



Figure 42: Co-pilot



Figure 43: Working area

Therefore, the ground manoeuvring area includes take-off and landing zones and areas for equipment management (Figure 43), it accommodates also the PIC and the co-pilot.

The Mobile Research Unit (UMR, Figure 4) is the ground infrastructure that ensures the robustness of the command and control system and it guarantees the communications between all the subsystems. In fact, in some remote investigation areas, some utilities, such as electricity and internet, are unavailable.

The UMR includes three technical compartments: one for transporting equipment, one for processing data acquired by the drone (Figure 46), and one for command and control operations (Figure 45).

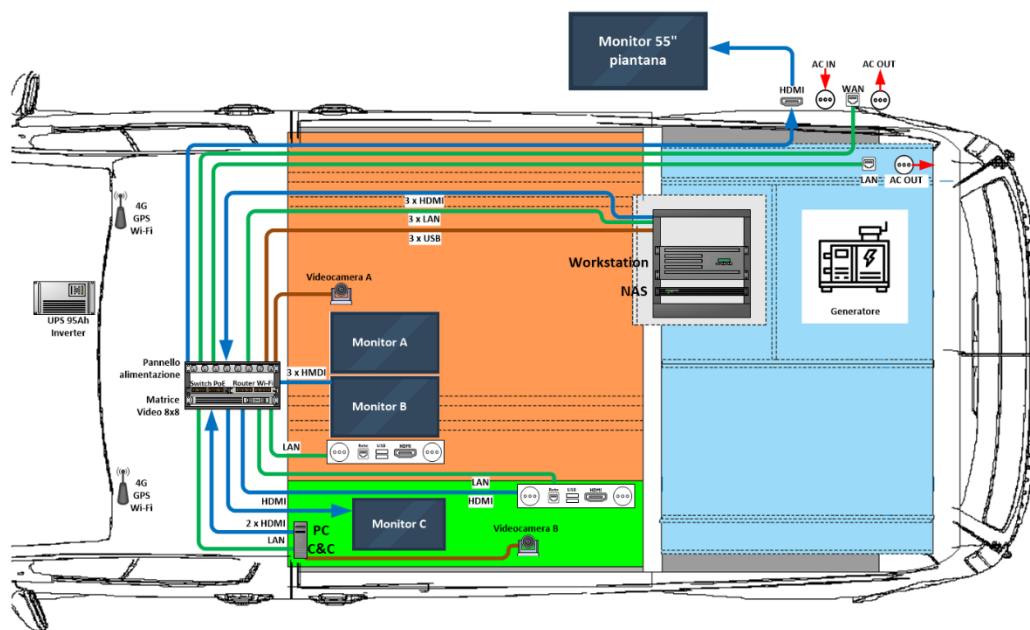


Figure 44: UMR



Figure 45: UMR – Command e Control Area



Figure 46: UMR – Elaboration room

## 2.2.9 Data and Method

### 2.2.9.1 Study Area

The ITINERIS project aims to develop an interdisciplinary research in environmental sciences through the use and reuse of existing data, services and new observations. To address scientifically and socially research questions, like the sustainable use of natural resources, implementation of nature-based solutions, green economy, pollution reduction, management and restoration of critical zones and ecosystems, carbon cycle, and mitigation of downstream effects of climate and environmental changes.

To test the system and implement usage procedures, the study area of the Migliarino, San Rossore, Massaciuccoli Regional Park Authority was selected, where the CNR IGG has already conducted aerial and ground monitoring.

The identified area is ideal for testing the drone and sensors (RGB HR, thermal, and multispectral), as it represents the appropriate ecosystem variability expected during all the operational monitoring procedures. Figure 47 illustrates the area of interest, including the drone's take-off and landing points:

- Point 1: 43°43'30.19"N; 10°16'49.66"E
- Point 2: 43°43'30.53"N; 10°16'39.61"E
- Point 3: 43°44'5.29"N; 10°16'25.17"E
- Point 4: 43°44'36.23"N; 10°16'37.69"E
- Point 5: 43°44'34.40"N; 10°16'58.64"E

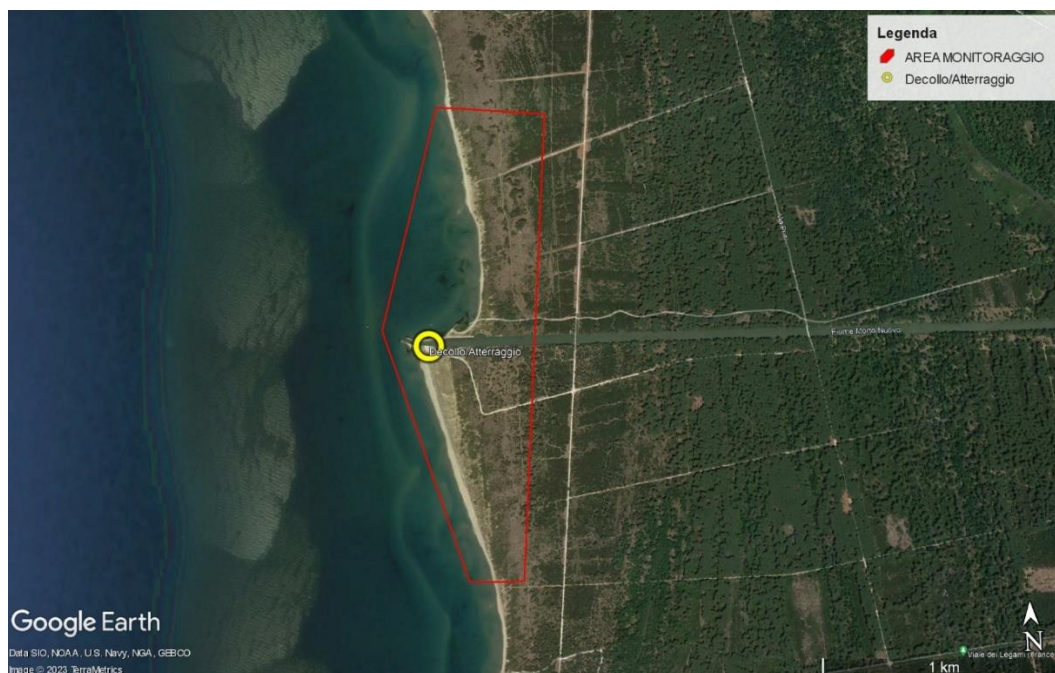


Figure 47: Study Area

The area measures 2000 m in length and 900 m in width, covering a total of 180 hectares. The airspace volume is restricted to a maximum flight altitude of 60 m, beyond which UAV flights are not allowed according to European and National regulations (Figure 48). In this regard all flights will be conducted at this maximum altitude, even though it is not fully optimal for a fixed-wing system.



Figure 48: Air space - <https://www.d-flight.it/web-app/>

### 2.2.9.2 Planning and Flight

During the test phases, numerous flights were conducted to assess system functionality and familiarise with flight planning.

After field training, acquisition flights were executed. Two types of flights were planned (Figure 49) at the maximum cruising altitude of 60 m: Area scan mode with the Altum-PT sensor and Corridor mode with the iXM RGB 100MP camera.

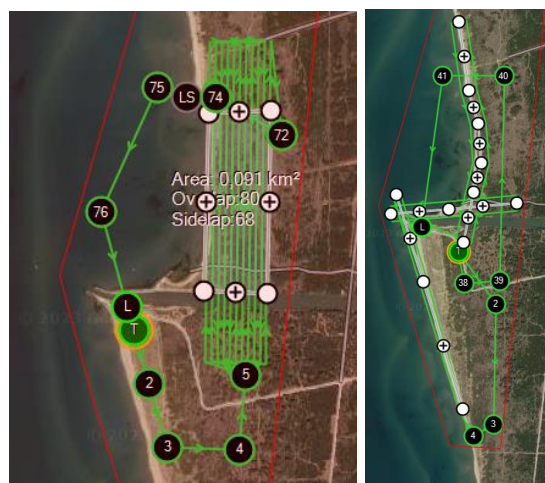


Figure 49: SX: Area mapping DX: Corridor Mapping

Both flight plans required a 70% frame overlap (frontal and lateral). With the adopted fixed-wing system SongBird, significant manoeuvring space was needed to transition between consecutive parallel transects and given the high lateral overlap, an alternative acquisition sequence was adopted. For instance, in the case seven transects, the execution procedure could be 1, 4, 7, 2, 6, 3, and 5. This concept is illustrated in Figure 50. This strategy allows the drone to be always aligned, during both pitch and roll acquisition phases. This prevents several issues during the image processing step.

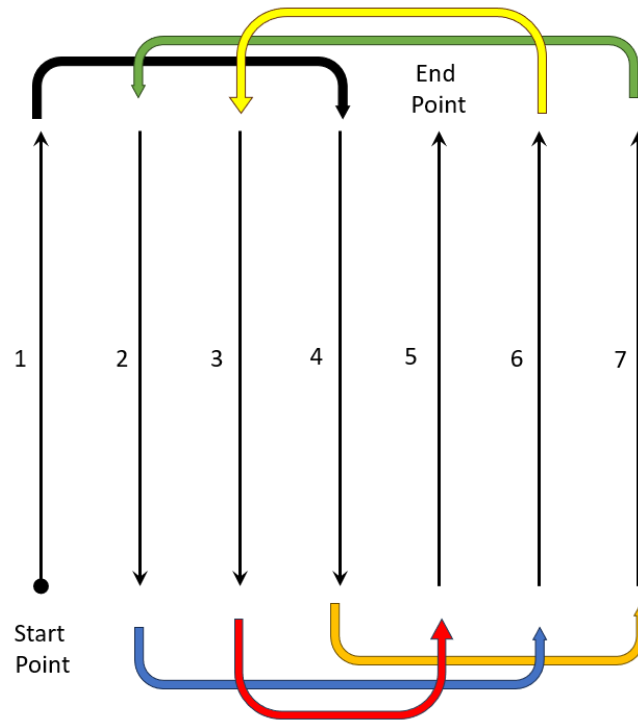


Figure 50: Execution Sequence

### 2.2.9.3 Data set RGB

The flight plan covered 31 hectares, captured in 11 minutes of flight at an altitude of 60 m AGL (Above Ground Level) using the PHASEONE iXM 100MP camera.

The dataset is made of 808 JPEG images derived from raw acquisition images. The raw images require a total of 52.6 GB of space while the extracted JPEG a total of 11.6 GB. Each image includes also GPS data in the EXIF file, enabling the creation of accurate georeferenced orthophotos, where the theoretical ground pixel resolution is 6 mm/pixel. The directory size, including the processing project executed with Agisoft Metashape, is 101.2 GB.

Considering the drone's real flight autonomy of 50 minutes at 60m AGL of altitude made with the PHASEONE iXM 100MP camera, a dataset of 125 hectares is produced with a total of 408 GB (RAW, JPEG, and processing project).

#### 2.2.9.4 Data set MULTIPARAMETRIC

The flight plan covered 18 hectares, captured in 13 minutes of flight at an altitude of 60 m AGL using the MICASENSE ALTUM-PT camera.

The dataset includes 5726 RAW multilayer images divided into Blue, Green, Red, Red Edge, Near Infrared, Panchromatic, and Thermal bands. The RAW images require a total of 119 GB of space. Each image includes GPS data in the EXIF file for generating accurate georeferenced orthophotos. The theoretical ground pixel resolution is 100 mm/pixel for multispectral images and 160 mm/pixel for thermal images. The directory size, including the processing project executed with Agisoft Metashape, is 178 GB.

Given the drone's real flight autonomy of 50 minutes at 60 m AGL of elevation made with the MICASENSE ALTUM-PT camera, the dataset covers 70 hectares, with a total of 684 GB (RAW, JPEG, and processing project).

#### 2.2.9.5 Elaboration and Data Output

The Agisoft Metashape is an advanced digital modelling solution designed to create professional-quality content and objects from remote sense images. The ultimate goal of Metashape is to generate textures, 3D models, and orthophotos using photographic data. Based on the latest multi-view 3D reconstruction technology, it operates with arbitrary images and is effective under both controlled and uncontrolled conditions. Photos can be taken from any position, and the object to be reconstructed must be visible in multiple photos. Both image alignment and 3D model reconstruction are fully automated.

The process, from acquiring photographic material to generating the 3D model, is divided into five main stages:

1. **Camera Alignment:** Metashape identifies common points across photographs, calculates, and determines the camera position for each image, refining the camera calibration parameters. The result is a sparse point cloud and a set of camera positions. The sparse point cloud represents photo alignment results, and it is not directly used in the subsequent 3D model construction procedure (except for the sparse cloud-based reconstruction method), and the data can be exported for external use. While, the camera positions are essential for further 3D modelling.
2. **Dense Point Cloud Construction:** Based on the estimated camera positions, Metashape generates a dense point cloud. This point cloud can be edited and classified before export or before generating the 3D model mesh.
3. **Mesh Construction:** Metashape reconstructs a 3D polygonal mesh representing the object, using the dense point cloud derived from measurements of the object's surface.
4. **Texture Mapping, DEM, and Orthophoto Generation:** The reconstructed geometry (mesh) can be textured or used to generate Digital Elevation Models (DEM) and orthophotos.
5. **Radiometric Calibration:** Radiometric calibration of multispectral and thermal images is conducted using a reference panel (Figure 51), photographed before and after the flight



Figure 51: Calibration target

### RGB Orthophoto

The alignment of 734 RGB images of 808 input images, resulted in a sparse point cloud of 700,280 points and a dense cloud of 419,372,522 points. Processing was conducted on a medium computing power setup, and it has required 4 hours and 25 minutes.

The reconstructed area measures 34.4 hectares, with an orthophoto resolution of 6.51 mm/pixel and a DEM resolution of 2.6 cm/pixel (Figure 52). The RGB orthophoto size is 25.86 GB, while the DEM is 2.44 GB. Both are georeferenced in the EPSG 4326 coordinate reference system.



Figure 52: RGB Orthophoto and DEM

Obtaining high resolution in both the RGB orthophotos and the corresponding DEM allows you to proceed with both identification and geometric analyses.

### Multispectral Orthophoto

Unlike RGB images, where each single shot produces a single layer, the use of multiparametric sensors allows for multiple layers for each shot. The processing workflow was divided into two parts: one for the single thermal layer and one utilizing five co-registered channels (Figure 53). In the latter case, the first channel was used for the processing workflow, while the export process combines all the five channels.

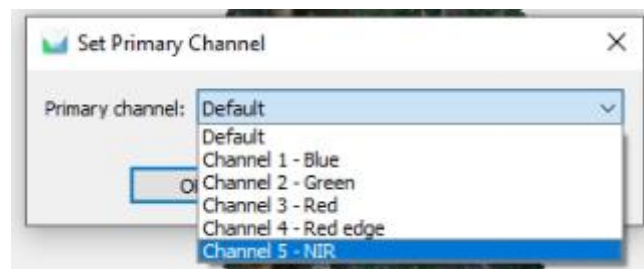


Figure 53: Channel

### Thermal Frame Processing

From the alignment of 799 RGB images of 828 input images, a sparse point cloud with 31,185 points and a dense point cloud with 144,494 points were obtained. Processing was completed with medium computational power in just 5 minutes. The reconstructed area covered 17.8 hectares, with a thermal orthophoto resolution of 16.3 cm/pixel and a DEM resolution of 65.3 cm/pixel. The thermal orthophoto size is 338 MB, while the DEM is 2.33 MB. Both were generated in the EPSG 4326 coordinate reference system.

To obtain a raster in temperature, the following transformation was applied:

$$\text{Pixel}_t = (\text{Pixel}_{dn}/100)-273.15$$

Where:

t: temperatura

dn; digital number

### Multispectral Frame Processing

From the alignment of 4,120 multispectral images of 4,140 input images, a sparse point cloud with 2,377,136 points and a dense point cloud with 23,996,957 points were obtained.

Processing took 2 hours and 20 minutes on medium computational power. The reconstructed area covered 19.5 hectares, with a multispectral orthophoto resolution of 2.64 cm/pixel and a DEM resolution of 10.5 cm/pixel (Figure 54).

The multispectral orthophoto size is 49.33 GB, while the DEM is 90 MB. Both were generated in the EPSG 4326 coordinate reference system.

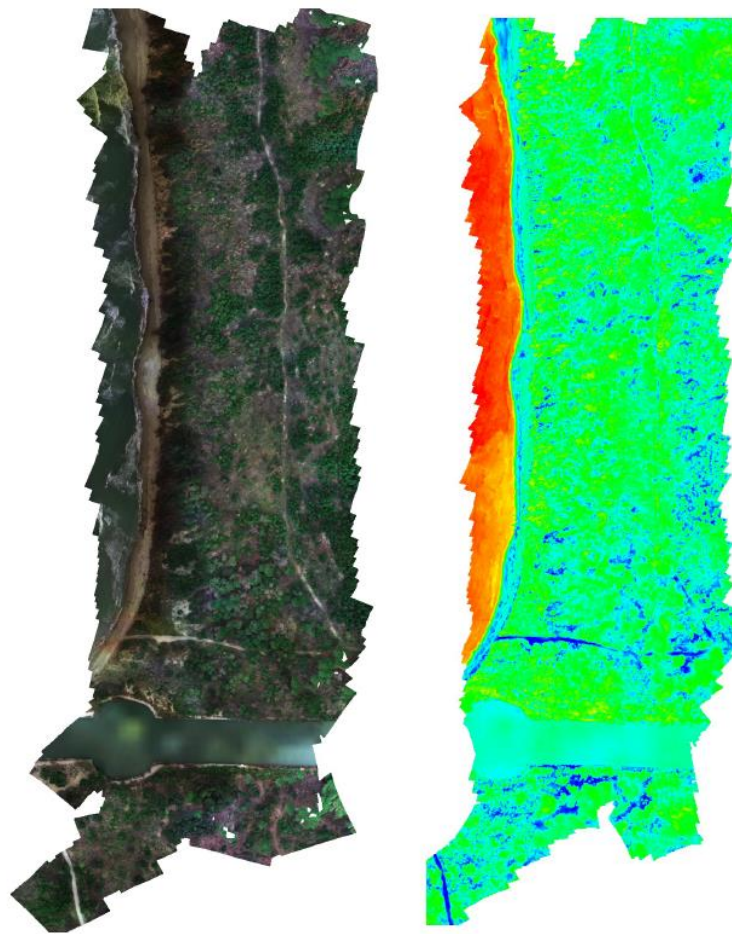


Figure 54: SX: Multi Ortophoto; DX: Termal Ortophoto

Combining layers from multispectral sensors provides complementary information to visible images. Several indices should be calculated (Figure 55):

- **NDVI (Normalized Difference Vegetation Index)**  
Measures chlorophyll content and evapotranspiration, indirectly indicating plant health:

$$NDVI = (NIR - RED)/(NIR + RED)$$

- **GNDVI (Green NDVI)**  
Uses the green band instead of red, indicating canopy density and potential water or nutrient deficiencies:

$$GNDVI = (NIR - GREEN)/(NIR + GREEN)$$

- **NDRE (Normalized Difference Red Edge)**  
Uses the red edge band (transition band between RED and IR) for late-stage crop maturity analysis, highlighting sugar and nitrogen content:

$$NDRE = (NIR - REDEEDGE)/(NIR + REDEEDGE)$$

- **LCI (Leaf Chlorophyll Index)**  
Assesses leaf chlorophyll, aiding in growth, health, and disease monitoring:

$$LCI = (NIR - REDEEDGE)/(NIR + RED)$$

- **SAVI (Soil Adjusted Vegetation Index)**  
Ideal for early growth stages, minimizing soil influence:

$$SAVI = (NIR - RED)/(NIR + RED + 0,16)$$

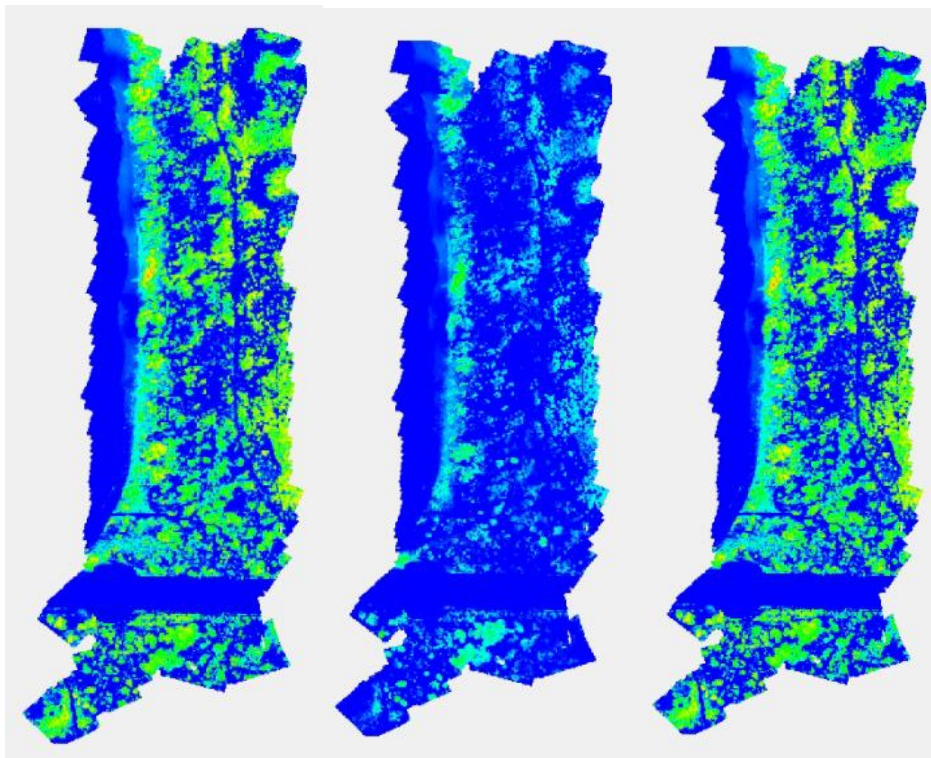


Figure 55: In sequence: NDVI; LCI; SAVI

These indices must be interpreted with knowledge of soil and vegetation characteristics. When cross-referenced, they provide detailed insights, supported by field measurements:

- Forestry: Estimation of biomass.
- Environmental Monitoring: Identification of soil and water pollution, buried waste, illegal landfills, and deforestation.
- Agriculture: Assessment of crop health and productivity.

### *2.2.9.6 Server and Data Sharing*

Actually, the produced data are stored and are available through a Network Attached Storage which is part of the Information and Communication Technologies (ICT) infrastructure developed by the m-WAVE laboratory (monitoring Water And earth oVer Earth) of the CNR-IGG. The m-WAVE laboratory is specialised in remote monitoring networks and already manages the ICT infrastructure for several IGG projects. It also supports the Critical Zone Virtual Research Environment (CZ-VRE) developed in the framework of the “ITINERIS” project.

In alignment with the actions of WP2, the produced data will be organised and made findable and usable for the scientific community. These data will follow the FAIR principles and will be described by means of metadata compliant with the EU INSPIRE Directive. Data will be:

- Findable, Accessible, and Reusable through the LifeWatch ERIC Metadata Catalogue, a GeoNetwork open-source platform.
- Harvested and made accessible through the ITINERIS HUB, a centralised access point offering a comprehensive collection of knowledge, data, analytical tools, and services provided by Italian Research Infrastructures (RIs). This hub focuses on the observation and study of environmental processes across the atmosphere, marine domain, terrestrial biosphere, and geosphere.

Although, through the ITINERIS Data Hub, it will be possible to discover metadata through a geospatial visualisation tool and get access to the datasets and digital products produced.

### 3 CONCLUSION

To reach the ITINERIS WP6 Task 6.15 goal, the analysis of bi-weekly drought events during the spring and summer months and their impact on vegetation greenness in northern Italy from 2000 to 2020 were conducted. To obtain drought risk maps for northern Italy, ground-based precipitation and temperature data and MODIS products were combined, for the first time at a spatial resolution of 1 km.

The findings revealed that despite northern Italy's historical abundance of water resources, multiple drought episodes have been observed since 2003. The research highlighted the importance of using multiple indices to study the complex phenomenon of drought. While significant positive temperature trends were noted in the region over the past two decades, the primary driver of drought events was the changing temporal distribution of precipitation. Analysing the spatial variability of the water balance proved to be a valuable tool for distinguishing between drought and non-drought years, with negative water balance values during droughts similar to those observed in southern Mediterranean regions.

Furthermore, this study provided the first correlation maps between bi-weekly vegetation indices (NDVI and EVI) and drought indices (SPI and SPEI). The correlations showed that in the Po Valley and Tuscan hills, vegetation types most affected by droughts were those heavily influenced by agriculture. In contrast, herbaceous communities and forests, if not heavily impacted by human activity, were less sensitive to drought and showed quicker recovery after drought events.

Furthermore, the results of this study emphasise the need for regional and high-resolution drought analysis. This can be achieved through the use of high-resolution remote sensing images, obtained via drone measurements of landscape and vegetation conditions.

In fact, studying satellite images, it is possible to cluster regions of interest. Individual clusters, which are smaller representative areas, can be monitored using UAVs equipped with high-autonomy and ultra-high-resolution sensors, such as VTOL systems.

In the first year of using the SongBirrd 150 system, the potential of a fixed-wing platform was demonstrated, allowing the acquisition of over 100 hectares per flight remaining within the 120-meter flight altitude limit set by European regulations. However, the volume of data to be managed and stored is substantial.

Storing and processing large numbers of frames requires significant computational costs, which can be reduced by increasing the flight altitude. At higher altitudes, larger areas can be monitored with the same number of frames. On the other hand, this reduce the resolution (e.g. transitioning from millimeters per pixel to centimeters per pixel with RGB sensors). Flying at an altitude of 200 meters AGL (Above Ground Level) can achieve a resolution of approximately 2.5 cm/pixel, which is still sufficient for comprehensive studies of phenomena and ecosystems.

A complex authorisation process is required to operate in shared airspace (above 120 meters), where both unmanned and manned aircraft are present. In low-population-density areas with unrestricted airspace, it may be possible in the near future to conduct low-environmental-impact acquisitions, ensuring the ability to capture increasingly larger areas per single flight.

## 4 BIBLIOGRAPHY

Acquaotta, F., Faccini, F., Fratianni, S., Paliaga, G., Sacchini, A. & Vilimek, V. (2019) Increased flash flooding in Genoa metropolitan area: a combination of climate changes and soil consumption? *Meteorology and Atmospheric Physics*, 131(4), 1099–1110. <https://doi.org/10.1007/s00703-018-0623-4>

Aguilar, E., Peterson, T.C., Obando, P.R., Frutos, R., Retana JA, Solera, M., Soley, J., Garcia, I.G., Araujo, R.M. and Santos, A.R. (2005) Changes in precipitation and temperature extremes in Central America and northern South America 1961–2003. *Journal of Geophysical Research: Atmospheres*, 110(D23107). <https://doi.org/10.1029/2005JD006119>.

Allen, R.G., Pereira, L.S., Raes, D. & Smith, M. (1998) Crop evapotranspiration: guidelines for computing crop water requirements. FAO irrigation and drainage paper 56. FAO Rome, 300, D05109.

Astiasari A, Hizbaron D and Setiawan M (2020) Estimation of land surface temperature in Dieng volcanic complex using tir-based satellite imageries. In IOP conference series: Earth and environmental science 45 (1).

Baronetti, A., Dubreuil, V., Provenzale, A. & Fratianni, S. (2022) Future droughts in northern Italy: high-resolution projections using EURO-CORDEX and MED-CORDEX ensembles. *Climatic Change*, 172(3), 1–22. <https://doi.org/10.1007/s10584-022-03370-7>

Baronetti, A., Gonzalez-Hidalgo, J.C., Vicente-Serrano, S.M., Acquaotta, F. & Fratianni, S. (2020) A weekly spatiotemporal distribution of drought events over the Po Plain (North Italy) in the last five decades. *International Journal of Climatology*, 40(10), 4463–4476. <https://doi.org/10.1002/joc.6467>

Baronetti, A., Acquaotta, F. & Fratianni, S. (2018) Rainfall variability from a dense rain gauge network in north-western Italy. *Climate Research*, 75(3), 201–213. <https://doi.org/10.3354/cr01517>

Beguiería, S., Vicente-Serrano, S.M., Beguiería, M.S. (2017) Package ‘SPEI’. Calculation of the standardised precipitation evapotranspiration index. <https://cran.r-project.org/web/packages/SPEI/SPEI.pdf> [Accessed 17th July 2023].

Bigi, A., Ghermandi, G. & Harrison, R.M. (2012) Analysis of the air pollution climate at a background site in the Po valley. *Journal of Environmental Monitoring*, 14(2), 552–563. <https://doi.org/10.1039/C1EM10728C>

Bradshaw, C.J.A. & Brook, B.W. (2014) Human population reduction is not a quick fix for environmental problems. *Proceedings of the National Academy of Sciences of the United States of America*, 111(46), 16610–16615. <https://doi.org/10.1073/pnas.1410465111>

Cardarelli, E., Meriggi, A., Brangi, A. & Vidus-Rosin, A. (2011) Effects of arboriculture stands on European hare *Lepus europaeus* spring habitat use in an agricultural area of northern. *Acta Theriologica*, 56(3), 229–238. <https://doi.org/10.1007/s13364-010-0019-4>

Ceppi, P., Scherrer, S.C., Fischer, A.M. & Appenzeller, C. (2012) Revisiting Swiss temperature trends 1959–2008. *International Journal of Climatology*, 32, 203–213. <https://doi.org/10.1002/joc.2260>

Chelli, S., Canullo, R., Campetella, G., Schmitt, A.O., Bartha, S., Cervellini, M. et al. (2016) The response of sub-Mediterranean grasslands to rainfall variation is influenced by early season precipitation. *Applied Vegetation Science*, 19(4), 611–619.

Diodato, N., Gomara, I., Baronetti, A., Fratianni, S. & Bellocchi, G. (2021) Reconstruction of erosivity density in northwest Italy since 1701. *Hydrological Sciences Journal*, 66(7), 1185–1196. <https://doi.org/10.1080/02626667.2021.1918696>

Fernández-Manjarrés J.F, Ruiz-Benito P, Zavala MA, Camarero JJ, Pulido F, Proença V, Navarro L, Sansilvestri R, Gande E, Marqués L, Temunović M, Bertelsmeier C, Drobinski P, Roturier S, Benito-Garzón M, García de Cortazar-Atauri I, Simon L, Dupas S, Levrel H and Sautier M (2018) Forest adaptation to climate change along steep ecological gradients: the case of the Mediterranean-temperate transition in South-Western Europe. *Sustainability* 10(9): 3065. <https://doi.org/10.3390/su10093065>

Fratianni, S. & Acquavota, F. (2017) The climate of Italy. In: Soldati, M. & Marchetti, M. (Eds.) *Landscapes and landforms of Italy*. World geomorphological landscapes. Cham, Switzerland: Springer, pp. 29–38. [https://doi.org/10.1007/978-3-319-26194-2\\_4](https://doi.org/10.1007/978-3-319-26194-2_4)

Fratianni, S., Cassardo, C. & Cremonini, R. (2009) Climatic characterization of Foehn episodes in Piedmont, Italy. *Geografia Fisica e Dinamica Quaternaria*, 32, 5–22.

García-Garizabal, I., Causapé, J., Abrahao, R. & Merchan, D. (2014) Impact of climate change on Mediterranean irrigation demand: historical dynamics of climate and future projections. *Water Resources Management*, 28(5), 1449–1462. <https://doi.org/10.1007/s11269-014-0565-7>

Gobiet, A., Kotlarski, S., Beniston, M., Heinrich, G., Rajczak, J. & Stoffel, M. (2014) 21st century climate change in the European Alps—a review. *Science of the Total Environment*, 493, 1138–1151. <https://doi.org/10.1016/j.scitotenv.2013.07.050>

Gonzalez-Hidalgo, J.C., Vicente-Serrano, S.M., Peña-Angulo, D., Salinas, C., Tomas-Burguera, M. & Beguería, S. (2018) High resolution spatio-temporal analyses of drought episodes in the western Mediterranean basin (Spanish mainland, Iberian Peninsula). *Acta Geophysica*, 66, 381–392. <https://doi.org/10.1007/s11600-018-0138-x>

Grossiord, C. (2020) Having the right neighbors: how tree species diversity modulates drought impacts on forests. *New Phytologist*, 228(1), 42–49. <https://doi.org/10.1111/nph.15667>

Gudmundsson, L. & Seneviratne, S.I. (2015) European drought trends. *Proceedings of the International Association of Hydrological Sciences*, 369, 75–79. <https://doi.org/10.5194/piahs-369-75-2015>

Halbac-Cotoara-Zamfir R, Smiraglia D, Quaranta G, Salvia R, Salvati L and Giménez-Morera A (2020) Land degradation and mitigation policies in the Mediterranean region: A brief commentary. *Sustainability*, 12(20): 8313. <https://doi.org/10.3390/su12208313>.

Hargreaves, G.H. & Samani, Z.A. (1985) Reference crop evapotranspiration from temperature. *Applied Engineering in Agriculture*, 1(2), 96–99.

ISTAT (2015) *Annuario statistico italiano 2015*. Roma, Istituto Nazionale di Statistica, pp. 810. ISBN 978-88-458-1866-0

Karnieli A, Ohana-Levi N, Silver M, Paz-Kagan T, Panov N, Varghese D, Chrysoulakis N and Provenzale A (2019). Spatial and seasonal patterns in vegetation growth-limiting factors over Europe. *Remote Sensing*, 11(20): 2406. <https://doi.org/10.3390/rs11202406>.

Kitsara, G., Papaioannou, G., Papathanasiou, A. & Retalis, A. (2013) Dimming/brightening in Athens: trends in sunshine duration, cloud cover and reference evapotranspiration. *Water Resources Management*, 27(6), 1623–1633.

Galmés, J., Flexas, J., Savé, R. & Medrano, H. (2007) Water relations and stomatal characteristics of Mediterranean plants with different growth forms and leaf habits: responses to water stress and recovery. *Plant and Soil*, 290(1), 139–155. <https://doi.org/10.1007/s11104-006-9148-6>

Geijzendorffer, I.R., Regan, E.C., Pereira, H.M., Brotons, L., Brummitt, N., Gavish, Y. et al. (2016) Bridging the gap between biodiversity data and policy reporting needs: an essential biodiversity variables perspective. *Journal of Applied Ecology*, 53(5), 1341–1350. <https://doi.org/10.1111/1365-2664.12417>

Gouveia, C.M., Bastos, A., Trigo, R.M. & DaCamara, C.C. (2012) Drought impacts on vegetation in the pre and post-fire events over Iberian Peninsula. *Natural Hazards and Earth System Sciences*, 12, 3123–3137. <https://doi.org/10.5194/nhess-12-3123-2012>

Gouveia CM, Trigo RM, Beguería S and Vicente-Serrano SM (2017) Drought impacts on vegetation activity in the Mediterranean region: An assessment using remote sensing data and multi-scale drought indicators. *Global and Planetary Change* 151: 15-27.

Guenzi D, Acquaotta F, Garzena D, Baronetti A, Fratianni S (2019) An algorithm for daily temperature comparison: CoTemp-comparing series of temperature. *Earth Sci Inform* 13:205–210. <https://doi.org/10.1007/s12145-019-00414-y>

Guenzi, D., Acquaotta, F., Garzena, D. & Fratianni, S. (2017) CoRain: a free and open source software for rain series comparison. *Earth Science Informatics*, 10(3), 405–416. <https://doi.org/10.1007/s12145-017-0301-y>

Leberger, R., Geijzendorffer, I.R., Gaget, E., Gwelmami, A., Galewski, T., Pereira, H.M. et al. (2020) Mediterranean wetland conservation in the context of climate and land cover change. *Regional Environmental Change*, 20(2), 1–11. <https://doi.org/10.1007/s10113-020-01655-0>

Isbell, F., Craven, D., Connolly, J., Loreau, M., Schmid, B., Beierkuhnlein, C.T. et al. (2015) Biodiversity increases the resistance of ecosystem productivity to climate extremes. *Nature*, 526(7574), 574–577. <https://doi.org/10.1038/nature15374>

Lionello P (2012) *The Climate of the Mediterranean Region: From the Past to the Future*. Elsevier 502 pp. ISBN: 978-0-12-416042-2.

Longobardi, A., Buttafuoco, G., Caloiero, T. & Coscarelli, R. (2016) Spatial and temporal distribution of precipitation in a Mediterranean area (southern Italy). *Environmental Earth Sciences*, 75(3), 188–208.

Luterbacher J, Dietrich D, Xoplaki E, Grosjean M and Wanner H (2004) European seasonal and annual temperature variability, trends, and extremes since 1500. *Science* 303: 1499–1503. <https://doi.org/10.1126/science.1093877>.

Marchina, C., Natali, C., Fazzini, M., Fusetti, M., Tassinari, R. & Bianchini, G. (2017) Extremely dry and warm conditions in northern Italy during the year 2015: effects on the Po river water. *Rendiconti Lincei*, 28(2), 281–290. <https://doi.org/10.1007/s12210-017-0596-0>

McKee, T.B.N., Doesken, J. & Kleist, J. (1993) The relationship of drought frequency and duration to timescales. In: *Proceedings of the Eighth Conference on Applied Climatology*. Boston: American Meteorological Society, pp. 179–184.

Musolino, D., De Carli, A. & Massarutto, A. (2017) Evaluation of socio-economic impact of drought events: the case of Po river basin. *European Countryside*, 9(1), 163–176. <https://doi.org/10.1515/euco-2017-0010>

Pavanelli, D. & Capra, A. (2014) Climate change and human impacts on hydroclimatic variability in the Reno River catchment, northern Italy. *CLEAN: Soil, Air, Water*, 42(5), 535–545. <https://doi.org/10.1002/clen.201300213>

Pogliotti, P., Guglielmin, M., Cremonese, E., Morra di Cella, U., Filippa, G., Pellet, C. et al. (2015) Warming permafrost and active layer variability at Cime Bianche, Western European Alps. *The Cryosphere*, 9(2), 647–661. <https://doi.org/10.5194/tc-9-647-2015>

Radic, V., Bliss, A., Beedlow, A.C., Hock, R., Miles, E. & Grahm Cogley, J. (2014) Regional and global projections of twenty-first century glacier mass changes in response to climate scenarios from global climate models. *Climate Dynamics*, 42, 37–58. <https://doi.org/10.1007/s00382-013-1719-7>

Rodrigo Comino J (2022) Desertification and degradation risks vs poverty: A Key Topic in Mediterranean Europe. *Geographical Research Letters* 48(1): 23-40. <http://doi.org/10.18172/cig.4850>.

San-Miguel-Ayanz, J., Durrant, T., Boca, R., Libertà, G., Branco, A., de Rigo, D., et al. (2018) *Forest fires in Europe, Middle East and North Africa 2017*. Joint Research Centre Technical Reports 140 pp. <https://doi.org/10.2760/663443> [Accessed 8th January 2023].

Schillinger WF, Schofstoll SE and Alldredge JR (2008) Available water and wheat grain yield relations in a Mediterranean climate. *Field Crops Research* 109 (1–3): 45–49. <https://doi.org/10.1016/j.fcr.2008.06.008>

Scocco, P., Piermarteri, K., Malfatti, A., Tardella, F.M. & Catorci, A. (2016) Effects of summer rainfall variations on sheep body state and farming sustainability in sub-Mediterranean pastoral systems. *Spanish Journal of Agricultural Research*, 14(3), e03SC02. <https://doi.org/10.5424/sjar/2016143-9230>

Shafran-Nathan, R., Svoray, T. & Perevolotsky, A. (2013) The resilience of annual vegetation primary production subjected to different climate change scenarios. *Climatic Change*, 118, 227–243. <https://doi.org/10.1007/s10584-012-0614-2>

Shirmohammadi-Aliakbarkhani, Z. & Saberali, S.F. (2020) Evaluating of eight evapotranspiration estimation methods in arid regions of Iran. *Agricultural Water Management*, 239, 106243. <https://doi.org/10.1016/j.agwat.2020.106243>

Sirangelo, B., Caloiero, T., Coscarelli, R. & Ferrari, E. (2017) Stochastic analysis of long dry spells in Calabria (southern Italy). *Theoretical and Applied Climatology*, 127(3–4), 711–724. <https://doi.org/10.1007/s00704-015-1662-0>

Tardella, F.M., Piermarteri, K., Malatesta, L. & Catorci, A. (2016) Environmental gradients and grassland trait variation: insight into the effects of climate change. *Acta Oecologica*, 76, 47–60. <https://doi.org/10.1016/j.actao.2016.08.002>

Tardella, F.M. & Catorci, A. (2015) Context-dependent effects of abandonment vs. grazing on functional composition and diversity of sub-Mediterranean grasslands. *Community Ecology*, 16(2), 254–266. <https://doi.org/10.1556/168.2015.16.2.13>

Thiébault, S. & Moatti, J.P. (2018) *The Mediterranean region under climate change: a scientific update*. IRD Editions Marseille.

Tirivarombo, S., Osupile, D. & Eliasson, P. (2018) Drought monitoring and analysis: standardised precipitation evapotranspiration index (SPEI) and standardised precipitation index (SPI). *Physics and Chemistry of the Earth*, 106, 1–10. <https://doi.org/10.1016/j.pce.2018.07.001>

Trucchia, A., Meschi, G., Fiorucci, P., Provenzale, A., Tonini, M. & Pernice, U. (2023) Wildfire hazard mapping in the eastern Mediterranean landscape. *International Journal of Wildland Fire*, 32, 417–434. <https://doi.org/10.1071/WF22138>

Turco M, Rosa-Cánovas JJ, Bedia J, Jerez S, Montávez JP, Llasat MC and Provenzale A (2018) Exacerbated fires in Mediterranean Europe due to anthropogenic warming projected with non-stationary climate-fire models. *Nature communications* 9(1): 1-9. <https://doi.org/10.1038/s41467-018-06358-z>.

Vallorani, R., Bartolini, G., Betti, G., Crisci, A., Gozzini, B., Grifoni, D. et al. (2018) Circulation type classifications for temperature and precipitation stratification in Italy. *International Journal of Climatology*, 38(2), 915–931. <https://doi.org/10.1002/joc.5219>

Vicente-Serrano SM, Azorin-Molina C, Peña-Gallardo M, Tomas-Burguera M, Domínguez-Castro F, Martín-Hernández N, Beguería S, El Kenawy A, Noguera I and García, M. (2019). A high-resolution spatial assessment of the impacts of drought variability on vegetation activity in Spain from 1981 to 2015. *Natural Hazards and Earth System Sciences* 19(6): 1189-1213. <https://doi.org/10.5194/nhess-19-1189-2019>.

Vicente-Serrano, S.M., Azorin-Molina, C., Sanchez-Lorenzo, A., Revuelto, J., Lopez-Moreno, J.I., Gonzalez-Hidalgo, J.C. et al. (2014) Reference evapotranspiration variability and trends in Spain, 1961–2011. *Global and Planetary Change*, 121, 26–40. <https://doi.org/10.1016/j.gloplacha.2014.06.005>

Vicente-Serrano, S.M., Azorin-Molina, C., Sanchez-Lorenzo, A., Revuelto, J., Lopez-Moreno, J.I., Gonzalez-Hidalgo, J.C. et al. (2014) Reference evapotranspiration variability and trends in Spain, 1961–2011. *Global and Planetary Change*, 121, 26–40. <https://doi.org/10.1016/j.gloplacha.2014.06.005>

Vissio, G., Turco, M. & Provenzale, A. (2023) Testing drought indicators for summer burned area prediction in Italy. *Natural Hazards*, 116, 1125–1137. <https://doi.org/10.1007/s11069-022-05714-z>

von Keyserlingk, J., de Hoop, M., Mayor, A.G., Dekker, S.C., Rietkerk, M. & Foerster, S. (2021) Resilience of vegetation to drought: studying the effect of grazing in a Mediterranean rangeland using satellite time series. *Remote Sensing of Environment*, 255, 112270. <https://doi.org/10.1016/j.rse.2020.112270>

Zimmermann, N.E., Gebetsroither, E., Zuger, J., Schmatz, D. & Psomas, A. (2013) Future climate of the European Alps. In: Cerbu, G. (Ed.) *Management strategies to adapt alpine space forests to climate change risks*. Rijeka: Tech, pp. 27–36. <https://doi.org/10.5772/56278>

Wallace, J.M. & Gutzler, D.S. (1981) Teleconnections in the geopotential height field during the northern hemisphere winter. *Monthly Weather Review*, 109(4), 784–812.

Commission Implementing Regulation (EU) 2019/947. <https://www.easa.europa.eu/en/document-library/regulations/commission-implementing-regulation-eu-2019947>

Commission Delegated Regulation (EU) 2019/945. <https://www.easa.europa.eu/en/document-library/regulations/commission-delegated-regulation-eu-2019945>

Germandrones GmbH, Alt-Moabit 55 DE-10555 Berlin, germandrones.com, Songbird Manual version 3.2.2

Micasense Altum-PT Integration Guide, <https://support.micasense.com/hc/en-us/articles/4419868608407-Altum-PT-Integration-Guide>

PHASEONE ixm-100MP <https://www.phaseone.com/solutions/geospatial-solutions/components/ixm-100/>